IT'S YOUR TIME
BE PRECISE

STANDARD IMAGING

Every day we spend **our time** optimizing ways to make QA easy and reliable.

Ask us how our solutions **can benefit you.**

WWW.STANDARDIMAGING.COM

Principles and applications of multienergy CT: Report of AAPM Task Group 291

Cynthia H. McCollough[a)]
Mayo Clinic, 200 First Street SW, Rochester, MN 55905, USA

Kirsten Boedeker
Canon (formerly Toshiba) Medical Systems Corporation, 1440 Warnall Ave, Los Angeles, CA90024, USA

Dianna Cody
University of Texas, M.D. Anderson Cancer Center, 7163 Spanish Grant, Galveston, TX 77554-7756, USA

Xinhui Duan
Southwestern Medical Center, University of Texas, 5323 Harry Hines Blvd, Dallas, TX 75390-9071, USA

Thomas Flohr
Siemens Healthcare GmbH, Siemensstr. 3, Forchheim, BY 91031, Germany

Sandra S. Halliburton
Philips Healthcare, 100 Park Ave, Suite 300, Orange, OH 44122, USA

Jiang Hsieh
GE Healthcare Technologies, 3000 N. Grandview Blvd. W-1190, Waukesha, WI 53188, USA

Rick R. Layman
University of Texas, M.D. Anderson Cancer Center, 7163 Spanish Grant, Galveston, TX 77554-7756, USA

Norbert J. Pelc
Stanford University, 443 Via Ortega, Room 203, Stanford, CA 94305-4125, USA

In x-ray computed tomography (CT), materials with different elemental compositions can have identical CT number values, depending on the mass density of each material and the energy of the detected x-ray beam. Differentiating and classifying different tissue types and contrast agents can thus be extremely challenging. In multienergy CT, one or more additional attenuation measurements are obtained at a second, third or more energy. This allows the differentiation of at least two materials. Commercial dual-energy CT systems (only two energy measurements) are now available either using sequential acquisitions of low- and high-tube potential scans, fast tube-potential switching, beam filtration combined with spiral scanning, dual-source, or dual-layer detector approaches. The use of energy-resolving, photon-counting detectors is now being evaluated on research systems. Irrespective of the technological approach to data acquisition, all commercial multienergy CT systems circa 2020 provide dual-energy data. Material decomposition algorithms are then used to identify specific materials according their effective atomic number and/or to quantitate mass density. These algorithms are applied to either projection or image data. Since 2006, a number of clinical applications have been developed for commercial release, including those that automatically (a) remove the calcium signal from bony anatomy and/or calcified plaque; (b) create iodine concentration maps from contrast-enhanced CT data and/or quantify absolute iodine concentration; (c) create virtual noncontrast-enhanced images from contrast-enhanced scans; (d) identify perfused blood volume in lung parenchyma or the myocardium; and (e) characterize materials according to their elemental compositions, which can allow in vivo differentiation between uric-acid and non-uric-acid urinary stones or uric acid (gout) or non-uric-acid (calcium pyrophosphate) deposits in articulating joints and surrounding tissues. In this report, the underlying physical principles of multienergy CT are reviewed and each of the current technical approaches are described. In addition, current and evolving clinical applications are introduced. Finally, the impact of multienergy CT technology on patient radiation dose is summarized. © *2020 American Association of Physicists in Medicine* [https://doi.org/10.1002/mp.14157]

Key words: dual-energy CT, material decomposition, material selective, multienergy CT, virtual monoenergetic, virtual noncontrast

Table of Contents

1. INTRODUCTION

This report has been reviewed and approved by the Computed Tomography (CT) Subcommittee, Imaging Physics Committee, Science Council and Executive Committee of the AAPM.

The charge for this task group was to prepare a report that teaches the fundamental principles of multienergy CT, describes current manufacturer implementations, introduces the various clinical applications available on specific systems, and addresses dosimetric considerations. The AAPM CT subcommittee commissioned this report to provide an authoritative open-access review of the topic for educational purposes.

The intended audience for this report includes medical physicists, radiologists, CT technologists, and other interested parties, including end-users of multienergy CT images, such as referring clinicians and radiation oncology physicians, physicists, and dosimetrists.

2. CLINICAL MOTIVATION FOR MULTIENERGY CT

CT scanners form images of a material's linear attenuation coefficient, normalized by that of water and displayed in units called Hounsfield Units (HU). The linear attenuation coefficient of a tissue depends on its chemical composition (effective atomic number, Z_{eff}), mass density (ρ), and the effective energy of the x-ray beam. The mass attenuation coefficient is defined as the linear attenuation coefficient of a material divided by its mass density, and is dependent only on the material's chemical composition and effective x-ray energy. Generally, higher atomic number and higher mass density lead to higher measured CT numbers at a given x-ray energy. It is possible for two different materials to have the same CT numbers if one has a higher effective atomic number but the other has a higher mass density. However, while the effect of mass density on CT numbers is independent of energy, the effect of effective atomic number varies significantly with photon energy. Thus, if measurements are made at multiple energies it is possible to decouple the influence of mass density and chemical composition on the CT number.

The fact that CT scans performed at multiple energies could be used to provide additional information regarding material composition is not a new discovery. Indeed, in his 1973 paper, Hounsfield wrote "Two pictures are taken of the same slice, one at 100 kV and the other at 140 kV... so that areas of high atomic numbers can be enhanced... Tests carried out to date have shown that iodine (Z = 53) can be readily differentiated from calcium (Z = 20)".[1]

For materials with the same effective atomic number as water, the CT number is independent of energy and quantitatively should reflect the density difference between the material and water. This is because CT numbers are defined with respect to the attenuation of water for a given x-ray spectrum. For any other material, the CT number will be energy dependent, making the physical interpretation of the CT number at a single energy ambiguous, as it could be caused by a density or chemical composition difference. If one wants to extrapolate the measured CT number to calculate the attenuation coefficient of the material at another energy, for example to use for attenuation correction in SPECT or PET or for dosimetry in radiation therapy, assumptions regarding material composition would need to be made, potentially leading to erroneous results.

Multienergy CT can decompose the measured attenuation into quantities that, unlike CT numbers, are independent of the x-ray energy. For example, materials with a higher effective atomic number than water will have increased CT numbers at lower energies. Conversely, materials with a lower effective atomic number than water will have lower CT numbers at lower energies. This behavior is expected for materials with low to moderate atomic number (e.g., <50) in the diagnostic CT energy range (>30 keV). Higher atomic number materials can have their K absorption edge (K-edge) within the measured spectrum, and the discontinuity in their attenuation coefficient at the K-edge can allow very specific measurement of their concentration.

The same physical principle that causes the meaning of CT numbers at a single energy to be ambiguous also causes beam hardening artifacts. CT systems use polychromatic x-ray beams, and the photons at the various energies experience energy dependent attenuation. Calibration of attenuation with a single material allows correction for beam hardening as long as the attenuation was caused by materials of similar atomic number. When that is not the case (e.g., regions containing both soft tissue and bone), this correction is inadequate and artifacts can result. Multienergy CT can better account for the polychromatic spectrum, allowing for improved beam-hardening correction.

Thus, the motivation for multienergy CT includes: (a) characterization of fundamental physical quantities that determine photon attenuation (mass or electron density and effective atomic number), (b) separation of materials that may have the same CT number at a single energy, (c) improvement in quantitative accuracy, (d) extrapolation of photon attenuation to other energies (e.g., for attenuation correction of radionuclide images or radiotherapy treatment planning), (e) quantitation of contrast agent concentration, perhaps even for multiple agents simultaneously, (f) characterization of materials for diagnostic specificity or image segmentation, (g) accurate correction of beam-hardening effects, and (h) increased conspicuity of iodinated contrast agent.

3. PHYSICAL PRINCIPLES OF MULTIENERGY CT

3.A. Dependence of x-ray attenuation on Z, density, and x-ray energy

Multienergy CT relies on the fact that x-ray attenuation characteristics are energy- and material-dependent. Without the energy-dependency, attenuation data collected with different energy spectra would not provide additional information. Without the material-dependency, different types of materials could not be differentiated.

There are three types of interactions of x-ray photons with matter in the diagnostic energy range: photoelectric effect, Compton, and coherent scatter. The total mass attenuation coefficient, $(\mu/\rho)_{total}$, of a material is expressed as the summation of the mass attenuation coefficients of these interactions:

$$\left(\frac{\mu}{\rho}\right)_{Total} = \left(\frac{\mu}{\rho}\right)_{Photoelectric} + \left(\frac{\mu}{\rho}\right)_{Compton} + \left(\frac{\mu}{\rho}\right)_{Coherent}.$$

(1)

The three mass attenuation coefficients have different dependencies on the input x-ray photon energy. In Fig. 1, $\left(\frac{\mu}{\rho}\right)_{Photoelectric}$, $\left(\frac{\mu}{\rho}\right)_{Compton}$, and $\left(\frac{\mu}{\rho}\right)_{Coherent}$ for muscle tissue and cortical bone are plotted individually.[2] The graph is on a log-log scale for better visualization of the full dynamic range of these coefficients. Examining the mass attenuation coefficients of muscle [Fig. 1(a)], the following observations can be made. First, the contribution of coherent scatter is relatively small compared to either the photoelectric effect or Compton scatter in the x-ray energy range of CT. Consequently, this type of interaction is typically ignored in the discussion of multienergy CT; only photoelectric effect and Compton scatter are considered in the theoretical derivation of multienergy CT material decomposition. It is also observed that the photoelectric effect depends strongly on x-ray energy, and at the low energy range, this interaction dominates. As the x-ray energy increases, the contribution of the photoelectric effect reduces quickly. The energy dependence of Compton scatter over the x-ray energy range used in CT is much weaker. Thus, as the x-ray energy increases and the photoelectric interaction decreases, Compton scatter becomes the dominating interaction. Multienergy CT takes advantage of these characteristics to perform material differentiation and decomposition.

The observations made regarding muscle also hold in the case of cortical bone [Fig. 1(b)]. In addition, there is in general a strong dependency of mass attenuation coefficients on material (or effective atomic number, Z_{eff}). In comparing the attenuation characteristics of muscle and cortical bone, note the difference in the vertical scale between two graphs.

3.B. Requirement for multiple unique energy measurements

To demonstrate the requirement for multiple unique energy measurements, the following example is provided. First, a tissue characterization phantom (Model 467, Gammex, Middleton, WI) with a 10 mg/mL iodine/solid-water insert was placed at the 12 o'clock position and a 50 mg/mL calcium/solid-water insert was placed at the 6 o'clock position [Fig. 2(a)]. The phantom was scanned with 140 kV; the reconstructed image is shown in Fig. 2(b). Visually, the two inserts are indistinguishable. Without prior knowledge, one would draw the erroneous conclusion that both inserts are made of the same material. While this experiment was carefully designed such that the selected concentrations of iodine and calcium produced similar CT numbers at 140 kV, it demonstrates that by relying solely on a single energy image, it is not always possible to separate two different materials. Given the energy-dependent nature of x-ray attenuation, when the same phantom is scanned with 80 kV, the CT numbers of the inserts are very different, as shown in Fig. 2(c).

By examining the same object with two different energies, one can differentiate materials that might otherwise look identical.

The selection of 80 and 140 kV for this example allowed the two x-ray spectra to be different enough to take advantage of the energy-dependent nature of the mass attenuation coefficient (Fig. 1). If the energy spectra were too similar to each other, the attenuation difference between two materials might not be large enough to produce a signal difference that could be differentiated from the noise.[3]

3.C. Intuitive description of material decomposition

The example in Fig. 2 clearly shows that by scanning an object at two tube potentials (different energy spectra), one can differentiate materials having different effective atomic numbers. For better visualization of this concept, consider a coordinate system with the reconstructed CT numbers measured from images acquired with two different energy spectra as the x- and y-axis, and each material plotted in this two-dimensional space. For example, the reconstructed iodine insert with 10 mg/mL concentration scanned under 80 kV has a CT number of 400 HU and under 140 kV a CT number of 194 HU. 10 mg/mL iodine, therefore, has a characteristic coordinate of (400, 194) in the 80- and 140 kV space (dual-energy space). If a mixture made exclusively of iodine and a water-equivalent material is scanned with 80 and 140 kV and has CT numbers that land on the same coordinate, one can assert, with relative confidence, that the iodine/water mixture has a concentration of 10mg/ml. If an unknown material scanned with 80 kV and 140 kV has CT numbers that land on the same coordinate, one can assert that the unknown material has the same attenuation characteristics at all x-ray energies as iodine with 10 mg/mL concentration.

To determine whether the same material (e.g., iodine), but having different concentrations, can produce a well-recognized "signature" in this space to allow easy identification of the material, one could scan iodine inserts of different concentrations and plot the results in the dual-energy space, as shown in Fig. 3. These points form a straight line intersecting the origin when the background is water-equivalent. Similarly, calcium inserts with different concentrations also form a straight line. However, the slopes of these lines are different. Therefore, by looking at the slope of the line formed by the measured CT numbers in the dual-energy space, one can characterize the material of interest. The slope of a line in this coordinate system is frequently referred to as the CT number ratio (CTR). When iodine is mixed not with water but with blood, as in clinical practice, the line will not intersect the origin; however, the slope of the line will be similar.

To differentiate iodine from calcium, a small zone is placed around each material's line so that any point that falls inside the zone will be classified as the same material, since noise and other nonideal properties of CT systems will produce variations in the measured CT values. An example of this is shown in Fig. 3 (light blue zone for calcium and light orange zone for iodine). Without *a priori* information (e.g.,

system bias), a centerline is typically used to separate the two zones.

3.D. Mathematical description of material decomposition

The fundamental mathematical formulation can be traced back to 1976,[4] with many subsequent developments having taken place since.[5–7] Recalling the earlier discussion, the total mass attenuation coefficient of a particular material, $(\mu/\rho)_{total}$, can be considered to be the linear combination of the two primary mechanisms for x-ray attenuation in the diagnostic imaging energy range: photoelectric effect and Compton scatter. Both effects are functions of the x-ray photon energy E. If we denote the mass attenuation functions due to the photoelectric effect and Compton scatter by $f_p(E)$ and $f_c(E)$, respectively, the total mass attenuation coefficient can be described as:

$$\left(\frac{\mu}{\rho}\right)(E) = \alpha_p f_p(E) + \alpha_c f_c(E), \tag{2}$$

where α_p and α_c represent the energy-independent contributions of $\left(\frac{\mu}{\rho}\right)_{Photoelectric}$ and $\left(\frac{\mu}{\rho}\right)_{Compton}$, respectively, to the total attenuation. Ignoring the K-edge, $f_p(E)$ and $f_c(E)$ are known based on x-ray physics. To determine α_p and α_c, we need two measurements at two different photon energies: E_L (low-energy) and E_H (high-energy):

$$\left(\frac{\mu}{\rho}\right)(E_L) = \alpha_p f_p(E_L) + \alpha_c f_c(E_L),$$

and

$$\left(\frac{\mu}{\rho}\right)(E_H) = \alpha_p f_p(E_H) + \alpha_c f_c(E_H). \tag{3}$$

Given two measurements and two unknowns, we can solve for α_p and α_c. Each material-of-interest is now uniquely represented by (α_p, α_c) with the photoelectric and Compton effects as the basis by which to characterize a material.[8] If the material's K-edge has a significant contribution to the measurements, the K-edge effect needs to be included in the model and additional equations (and measurements) may be needed to solve for the unknowns.

The parametric fit model described above is known to have limited accuracy in describing real materials due to the fact that molecular interactions are ignored.[9] It can be shown that accuracy improves by instead using attenuation functions of real materials. From a routine clinical practice point of view, decomposition into physical interaction representations — photoelectric and Compton effects — does not provide a direct linkage to human anatomy, pathology, or physiology, making it difficult for a radiologist to interpret the resulting images. Since one objective of multienergy CT is to provide an easy way for radiologists to identify different materials, it is more convenient to use known-material attenuation functions as the basis of representation. For example, if water- and iodine-attenuation are used as the basis functions, other

materials are then represented as a mixture or linear combination of these two materials. This approach is often called material decomposition.[8]

To accomplish this, we need to replace the photoelectric and Compton functions, $f_p(E)$ and $f_c(E)$, by the mass attenuation functions of basis materials A and B, $(\mu/\rho)_A(E)$ and $(\mu/\rho)_B(E)$. From Eq. (2), the two sets of functions are related by

$$\left(\frac{\mu}{\rho}\right)_A (E) = \alpha_{A,p} f_p(E) + \alpha_{A,c} f_c(E)$$

and

$$\left(\frac{\mu}{\rho}\right)_B (E) = \alpha_{B,p} f_p(E) + \alpha_{B,c} f_c(E), \tag{4}$$

where $\alpha_{A,p}$, $\alpha_{A,c}$, $\alpha_{B,p}$, and $\alpha_{B,c}$ represent the contributions of the photoelectric and Compton effects for materials A and B respectively. Solving for $f_p(E)$ and $f_c(E)$, and substituting back into Eq. (2), we obtain:

$$\left(\frac{\mu}{\rho}\right)(E) = \frac{\alpha_p \alpha_{B,c} - \alpha_c \alpha_{B,p}}{\alpha_{A,p}\alpha_{B,c} - \alpha_{B,p}\alpha_{A,c}} \left(\frac{\mu}{\rho}\right)_A (E)$$
$$+ \frac{\alpha_c \alpha_{A,p} - \alpha_p \alpha_{A,c}}{\alpha_{A,p}\alpha_{B,c} - \alpha_{B,p}\alpha_{A,c}} \left(\frac{\mu}{\rho}\right)_B (E) \tag{5}$$
$$= \beta_A \left(\frac{\mu}{\rho}\right)_A (E) + \beta_B \left(\frac{\mu}{\rho}\right)_B (E).$$

β_A and β_B are energy independent, indicating that these coefficients are valid for all energies above the K-edge of both materials (note that the K-edge effect is ignored in the formulation of f_p and f_c). Equation (5) shows that the mass attenuation coefficient of a material can be represented as the linear combination of the mass attenuation coefficients of materials A and B. Materials A and B are often called the basis materials and are selected such that their effective atomic numbers Z_{eff} are sufficiently different to ensure different mass attenuation characteristics.

For illustration, consider a simple example of using two materials (water and iodine) to represent the attenuation characteristics of a third material (calcium). Figure 4 plots the

mass attenuation coefficients of three materials: iodine, calcium, and water, based on the NIST data.[10] The three curves look significantly different in terms of their shapes, especially with the K edges of the iodine and calcium. However, if we ignore the low-energy portion (orange shaded area of $E \leq 33.2$ keV), the three curves are quite similar. In fact, the mass attenuation coefficient of calcium can be approximated by a linear combination of the mass attenuation coefficients of iodine and water:

$$\left(\frac{\mu}{\rho}\right)_{calcium} \approx 0.835 \left(\frac{\mu}{\rho}\right)_{water} + 0.064 \left(\frac{\mu}{\rho}\right)_{iodine} . \tag{6}$$

Over the energy range of 33.2 keV $< E \leq 150$ keV, the measured and fitted calcium mass attenuation curves overlap nicely. A significant difference does exist for the energy range below the K-edge of iodine. However, most low-energy x-ray photons are removed from the beam by the prepatient filtration and the patient's body prior to reaching the CT detector, hence, the error caused by ignoring these low-energy photons is small.

Multiplying both sides of Eq. (5) by the mass density ρ yields

$$\mu(E_j) = \beta_A \left(\frac{\mu}{\rho}\right)_A (E_j)\rho + \beta_B \left(\frac{\mu}{\rho}\right)_B (E_j)\rho, \quad j = L, H,$$
$$= \left(\frac{\mu}{\rho}\right)_A (E_j)\rho_A + \left(\frac{\mu}{\rho}\right)_B (E_j)\rho_B, \quad j = L, H. \tag{7}$$

After acquiring two sets of data, one using a high-energy spectrum E_H and one using a low-energy spectrum E_L, and reconstructing two images from these data sets, solving Eq. (7) on a pixel by pixel basis yields images of the mass densities of materials A and B. This process is often called image-space material decomposition, since the entire process is carried out using reconstructed images.

The underlying assumption is that the reconstructed high- and low-energy images are accurate and are free of confounding effects, such as beam-hardening. Since such assumption is often violated, image-space decomposition algorithms
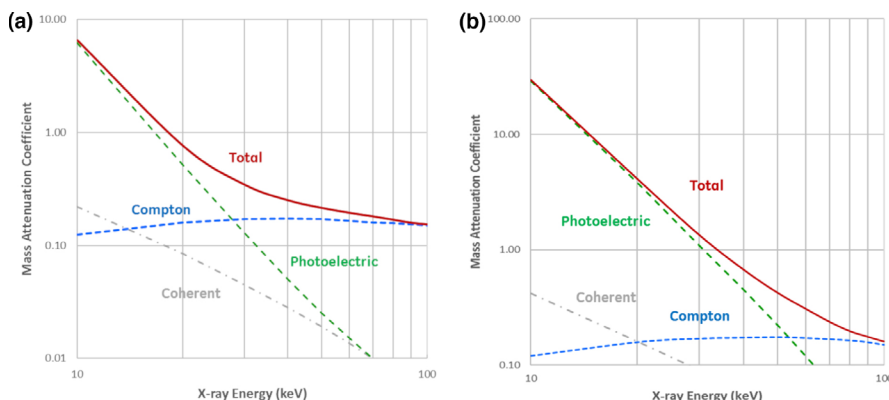

FIG. 1. Mass attenuation coefficients for muscle (a) and cortical bone (b). Note the log-log scale and that the range of attenuation values on the y-axis differs between muscle and cortical bone.
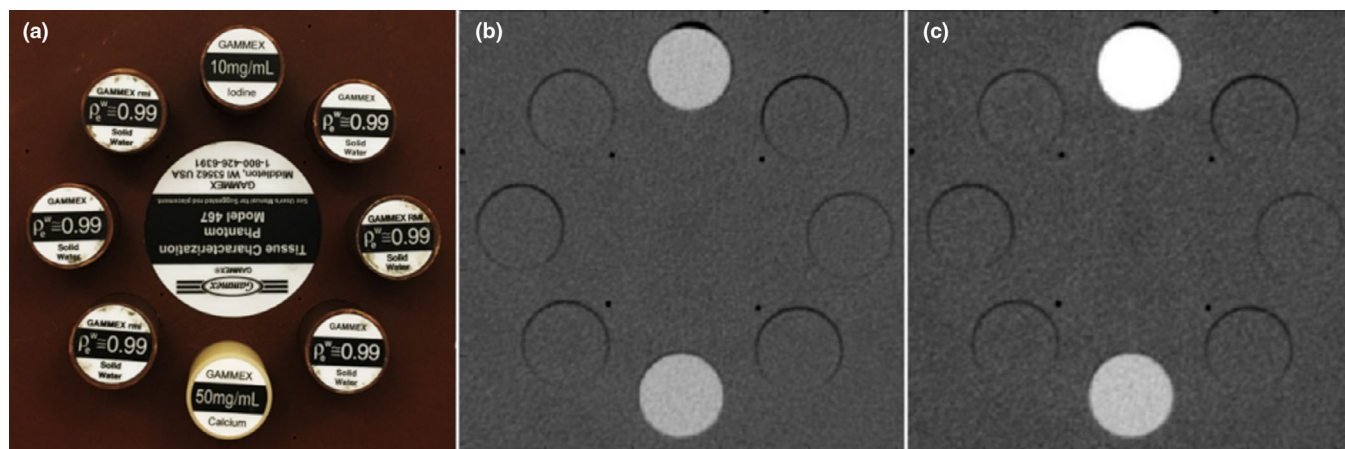
FIG. 2. Intuitive explanation of material differentiation with dual-energy computed tomography (WW = 500, WL = 100). (a) Model 467 Gammex phantom built from their "Solid Water®" plastic-like material, 10 mg/mL iodine (12 o'clock), and 50 mg/mL calcium (6 o'clock) inserts. (b) 140 kV image. (c) 80 kV image. All the other inserts are made of the same material as the background. Courtesy of Jiang Hsieh, PhD, GE Healthcare Technologies.

require that beam hardening and other sources of bias be carefully addressed during image reconstruction.

One common way to overcome inaccuracies due to effects such as beam-hardening is to perform the material decomposition in projection space; this is called projection-space decomposition.[4,6] This process is similar to the image-based material decomposition except that it is performed using the measured low- and high-energy projection data. The material decomposition process here must take into consideration the input x-ray beam spectral changes due to the presence of bowtie, beam-hardening effects present in the measured projections,[11] and spectral response of the CT detectors. When successfully implemented, projection-space material decomposition may provide improved quantitative accuracy.

Both image-space and projection-space decomposition techniques require consistency between the high- and low-energy data, both spatially and temporally. In general, any motion by or within the subject between the acquisition of the high- and the low-energy data may introduce artifacts and quantitative errors.

The discussion and example provided above explains the process of decomposing a material into two basis materials. In many clinical situations, however, it is desirable to decompose a mixture into three or more basis materials (often called three-material decomposition or multi-material decomposition). It is sometimes wrongly assumed that simply acquiring data using three different energies (spectra) allows decomposition into three different materials. However, unless one of the materials has a K-edge in the energy range of interest, such a decomposition is unstable because the attenuation curves are dominated by only two physical processes. Three material decomposition is possible with measurements at two different energies, but requires the use of additional information or supplemental constraints, such as having one material with a K-edge in the energy range of interest, assuming volume or mass conservation, or using precalibrated subregions in the low- and high-energy space.[12,13]

3.E. Challenges to accurate material decomposition

Given the close proximity of the iodine and calcium zones shown in Fig. 3, it is important that measured CT numbers are accurate. The area in the dual-energy space between the iodine and calcium regions decreases substantially as their respective concentrations are reduced. Additionally, the material classification task is impacted by the presence of statistical noise in the measured CT numbers and the amplification of such noise in the decomposition process.[4] Therefore, increased noise in the low- and high-energy images decreases the accuracy of the
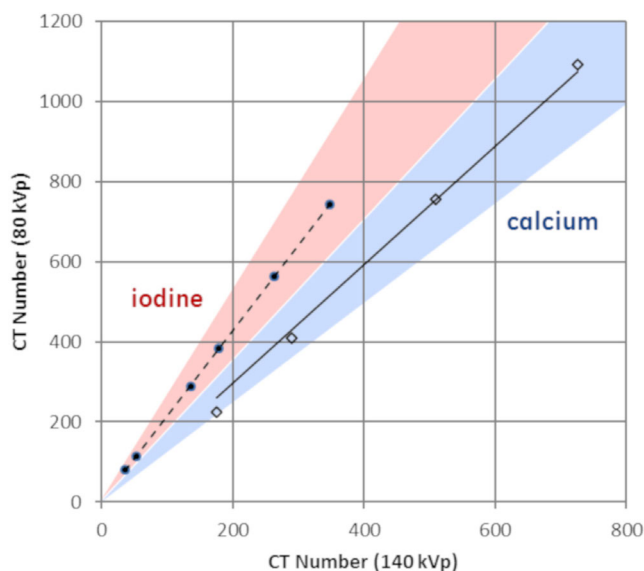
FIG. 3. Computed tomography number measurements of different concentrations of iodine/solid-water and calcium/solid-water inserts. Iodine concentrations (circles) were 2, 2.5, 7.5, 10, 15, and 20 mg/mL. Calcium concentrations (diamonds) were 50, 100, 200, and 300 mg/mL. The dual-energy space is shown here with the low-kV data on the y axis and the high-kV data on the x axis.[190] Courtesy of Jiang Hsieh, PhD, GE Healthcare Technologies.
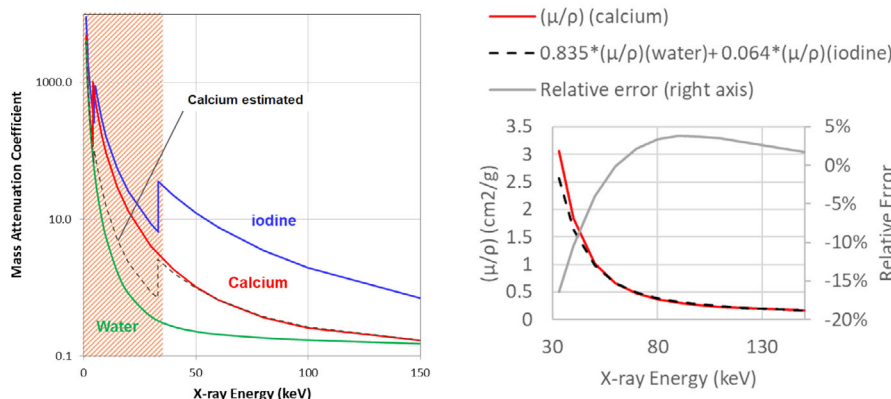
Fig. 4. (Left) Mass attenuation coefficients of water (green), calcium (red), iodine (blue), and the estimated mass attenuation coefficient of calcium using a linear combination of iodine and water (gray dotted line). Orange shaded area refers to E ≤ 33.2 keV (low-energy portion). (Right) Mass attenuation curves of $\left(\frac{\mu}{\rho}\right)_{calcium}$, $0.835\left(\frac{\mu}{\rho}\right)_{water}+0.064\left(\frac{\mu}{\rho}\right)_{iodine}$, and their relative errors in the energy range of 33.2 to 150 keV.

material separation. Even for a scan taken with high tube-current-time-product values and reconstructed with a larger image slice thickness, the impact of the noise is not negligible.[3] The separation of iodine and calcium, and hence the material classification performance, can be improved by increasing the difference in the two energies used for measurement, because this increases the difference between the slopes of the iodine and calcium lines in Fig. 3.[14]

In addition to noise, other factors can also impact the accuracy of the material decomposition process. For example, scatter can bias the measured CT numbers and may lead to erroneous material classification. Therefore, it is important to ensure that the impact of scatter is adequately mitigated, either with software corrections, or hardware designs such as a two-dimensional focused collimator.

Another dominant source of bias in multienergy CT material decomposition is beam-hardening. For single-energy CT, this phenomenon is well-understood and can be adequately corrected.[3] Beam hardening is most pronounced at lower photon energies, and hence stronger in the low-energy images compared to in the high-energy images. Since material differentiation performance relies on the accuracy of measured attenuation values in the individual low- and high-energy data sets, different amounts of beam hardening between the low- and high-energy data can result in increased bias in mass density values in the basis images.

3.E.1. Noise amplification

It can be shown that the material decomposition process amplifies noise,[15] for example, by reducing contrast-to-noise ratios. This phenomenon occurs regardless of whether projection-space or image-space material decomposition is performed. For illustration, Fig. 5 shows a Gammex phantom scanned with 80- and 140 kV, and reconstructed with a filtered back projection algorithm as shown by (a) and (b). The corresponding water (iodine)- and iodine (water)-density images are shown in (c) and (d). The material in parentheses indicates the other material of the basis pair. It is clear that

noise has increased significantly after the material decomposition process. Additional processing is typically applied to the material-specific images to suppress noise.

3.E.2. Noise correlation and opportunities for noise reduction

It should be pointed out that noise values in the water (iodine)- and iodine (water)-density images are not independent; they are negatively correlated.[15] Therefore, noise reduction processes can take advantage of these characteristics and avoid unnecessary degradation of spatial resolution. Noise-reduced water- and iodine-density images from the above example are shown in (e) and (f). Significant reduction in noise is observed. In addition, careful examination of the edges of the inserts shows minimum impact on the sharpness, or spatial resolution, of the images.

3.F. Synthetic images from multienergy CT

3.F.1. Virtual monoenergetic images

The results of material decomposition include energy-independent information that can be used to generate synthetic monoenergetic images, which are also referred to as virtual monoenergetic images or virtual mono-chromatic images. These images emulate the appearance of a CT study performed with a true monoenergetic photon source, for example, a synchrotron x-ray source. In principle, virtual monoenergetic images can be generated at any energy, but due to image quality limitations and other practical considerations, most multienergy CT platforms provide virtual monoenergetic images in the range 40 to 200 keV. Virtual monoenergetic images are available on all commercially available dual-energy CT platforms.

Virtual monoenergetic images are calculated by first determining the mass densities of materials A and B, using Eq. (7). The virtual monoenergetic image at energy E_m is generated by
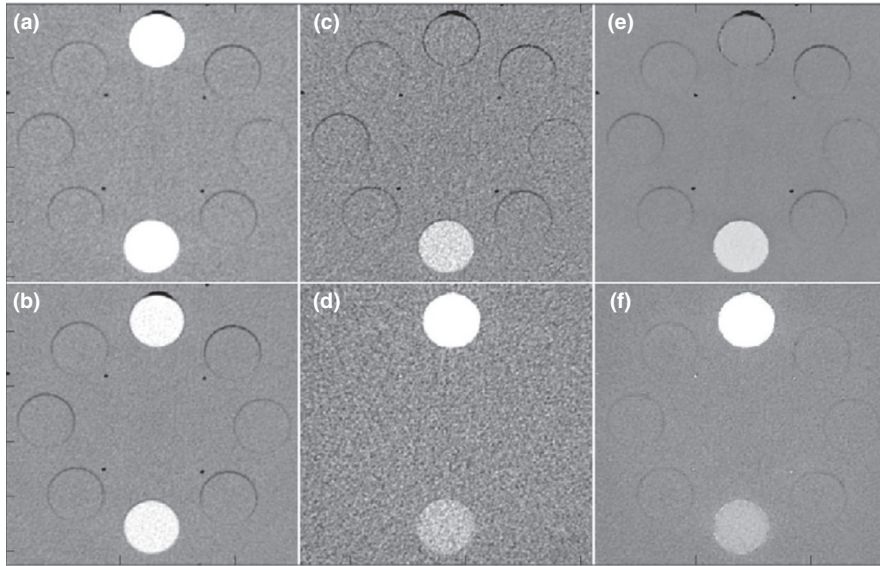
FIG. 5. Illustration of material decomposition impact on noise and noise compensation. (a) 80 kV image, (b) 140 kV image, (c) water (iodine)-density image, (d) iodine (water)-density image, (e) water (iodine)-density image with noise reduction, (f) iodine (water)-density image with noise reduction. Courtesy of Jiang Hsieh, PhD, GE Healthcare Technologies.

$$\mu(E_m) = \left(\frac{\mu}{\rho}\right)_A (E_m)\rho_A + \left(\frac{\mu}{\rho}\right)_B (E_m)\rho_B, \qquad (8)$$

where $(\mu/\rho)_{A,B}(E_m)$ is the mass attenuation coefficient for the basis materials A and B at energy E_m.

It has also been demonstrated that the monoenergetic image can be generated by the weighted sum of the low- and high-energy images, that is,

$$CT(E_m) = w(E_m)CT^L + (1 - w(E_m))CT^H, \qquad (9)$$

where "CT" is the CT number in the low (L) energy or high (H) energy image, and $w(E_m)$ is a weighting factor that depends on the desired monoenergetic energy (E_m) and the effective energies of the low- and high-energy acquisitions.[16]

Similarly, for material decomposition using the photoelectric and Compton Effect contributions, the virtual monoenergetic images can be generated by

$$\mu(E_m) = (\rho_p)f_p(E_m) + (\rho_c)f_c(E_m), \qquad (10)$$

where $f_p(E)$ and $f_c(E)$ are the functions describing the photoelectric and Compton mass attenuation coefficients, respectively, and ρ_p and ρ_c are the associated mass densities determined by the material decomposition.[4]

Projection space decomposition generates the sinogram of basis functions, for example, the sinogram of ρ_A and ρ_B in Eq. (7), or the sinograms of ρ_p and ρ_c in Eq. (10). One can reconstruct the sinograms to create basis-material mass density images (ρ_A and ρ_B, or ρ_p and ρ_c) and then convert them to virtual monoenergetic images in a manner similar to the image-space method discussed above, that is, Eqs. (8) or (10). Alternatively, the sinogram of the basis functions can be directly converted to the sinogram of a virtual monoenergetic image at energy E_m using

$$P(\mu(E_m)) = P(\rho_A)\left(\frac{\mu}{\rho}\right)_A (E_m) + P(\rho_B)\left(\frac{\mu}{\rho}\right)_B (E_m), \qquad (11)$$

where $P(\mu(E_m))$ is the sinogram of the virtual monoenergetic image; the virtual monoenergetic image is then created via CT reconstruction.[11]

Virtual monoenergetic images provide the most accurate CT numbers at the different virtual energy levels only for the two basis materials (e.g., water and iodine, or water and bone), other materials may have with less accurate CT numbers. Virtual monoenergetic images usually have different image noise levels at different energies.[16] A low-keV virtual monoenergetic image, for example, 50 keV, has dramatically increased noise compared with at higher energy levels, which can mitigate the benefit of increased iodine contrast in the low-keV image. CT manufacturers and investigators are continuing to develop improved algorithms to overcome this problem and make the noise more constant across the entire energy range.[17,18] A plot of image noise vs. virtual monoenergetic energy setting (keV value), both with and without (W/O) energy-domain noise reduction, is shown in Fig. 6.[18]

3.F.2. Material-specific or material-removed images

The results of material decomposition, for example, ρ_A and ρ_B in Eq. (7), is a material-specific image that can be presented as the distribution map of each material's mass density. The correct unit for the pixel values corresponding to mass density is mg/ml. However, using reasonable assumptions regarding material type and measurement energy spectra, some manufacturers convert the density information into CT numbers, in Hounsfield units, by multiplying the calculated mass density by the estimated mass attenuation
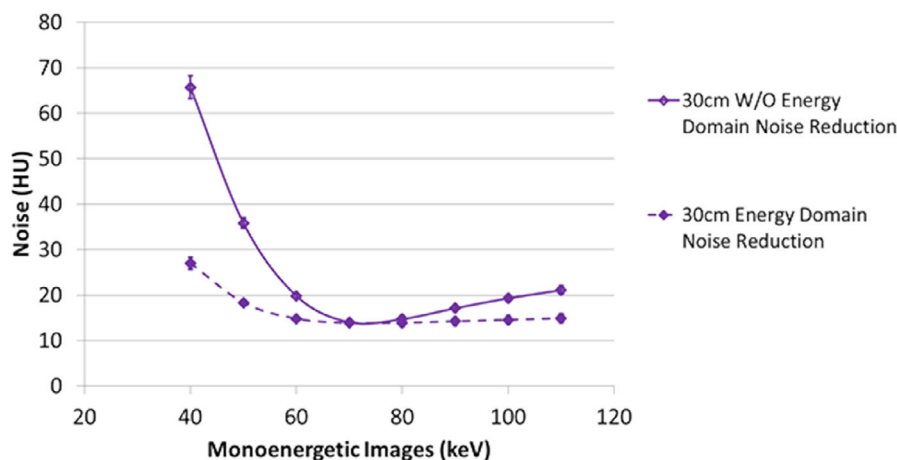
FIG. 6. Demonstration of the use of noise reduction to improve noise uniformity in virtual monoenergetic images across different energy (keV) settings. The dashed line provides more uniform noise values over the evaluated energy range than does the solid line due to the use of an energy-domain noise reduction technique.[17,18] Courtesy of Shuai Leng, PhD, Mayo Clinic.

coefficient to determine the estimated linear attenuation coefficient, and then converting that into Hounsfield units. This serves two purposes. First, Hounsfield units are more familiar to the majority of clinical users and second, PACs systems frequently misinterpret density information and display the pixel values in Hounsfield units. DICOM Supplement 188 was developed to ensure correct interpretation and display of multienergy CT data and address this problem. However, it has not yet been commercially implemented.

Depending on the clinical task, a variety of materials can be selected to generate material-specific or material-removed images. Common materials used are iodine and water, and their material-specific images are often referred to as iodine or water maps, respectively. Other commonly available image pairs include calcium and water images. Some manufacturers refer to images where iodine or calcium signal has been removed as virtual noncontrast or virtual noncalcium images, respectively.

In principle, dual-energy CT generates material-specific image pairs because two separate measurements, i.e., at low and high energies, are acquired, which is equivalent to solving for two unknowns using two equations. When there are more than two materials in the region of interest, either additional information is required or assumptions have to be made to solve the equations. Three material decomposition algorithms often have an assumption of volume or mass conservation, that is

$$f_1 + f_2 + f_3 = 1, \tag{12}$$

where f_1, f_2, and f_3 are the volume or mass fractions of the three components.[12] Based on volume conservation, the concept of the material decomposition can be intuitively explained as a geometric illustration (Fig. 7).[13]

Understanding the nature of the decomposed image is essential to the correct interpretation of material-decomposed images. This is particularly important since the naming conventions in commercial systems for material-specific or
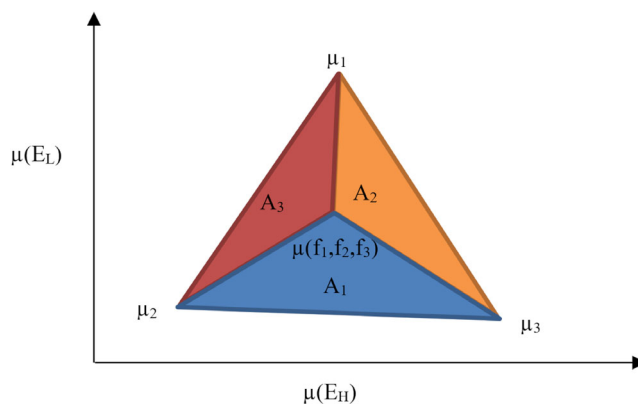
FIG. 7. Geometric explanation of three material decomposition based on volume conservation. The horizontal axis and vertical axis are the linear attenuation coefficients in the high- and low-energy images, respectively. Points μ_1, μ_2, and μ_3 locate the three basis materials in this space. A_1, A_2, and A_3 are the areas of the triangles. The unknown material μ lies inside the triangle (μ_1, μ_2, and μ_3) with volume fractions of (f_1, f_2, f_3), so $f_i = A_i/(A_1 + A_2 + A_3)$, $i = 1, 2, 3$.

material-removed images imply something that is not physically accurate, namely that "iodine images" contain *only* iodine signal and "water" or "soft-tissue images" contain *only* water or soft tissue.[19] In patients (unlike in simple iodine and water phantoms), when measured attenuation data have been decomposed into only two basis images (eg iodine and water), the resultant signal in a given voxel will contain signal from materials *other than the iodine and water basis materials* (eg fat or bone) that are physically present in that voxel. A common misconception is that measurements of iodine concentration in the iodine image are *equal* to the actual physical mass density (ie concentration) of iodine. Instead, all materials present, except those having attenuation properties equivalent to water, will contribute some signal to the iodine map. Likewise, all materials present, except those having attenuation properties equivalent to iodine, will contribute some signal to the water map.

Understanding this principle explains why bone is visible in the "iodine map," and why the CT number of fat in the water or soft-tissue image (commercially referred to as a "virtual noncontrast (VNC)" image) is different than in a conventional true noncontrast image."[19] For a water-iodine decomposition, the presence of bone or fat violates the assumption that only water and iodine are present in the image, neither of which are equivalent to bone or fat in terms of attenuation properties as energy is varied. Thus, bone or fat attenuation is represented partially in the "iodine-removed" or VNC image and the remaining component of bone or fat attenuation is represented in the "water-removed" image. Hence, bone will appear in both the "iodine image" and the "water or soft-tissue image." Also, since the VNC image accounts for only a portion of the fat attenuation, fat in a VNC image will have a different CT number than fat in a true noncontrast CT image. Of note, the decomposition may generate negative mass density values for fat, which although reasonable from a mathematical perspective, may be difficult to explain to clinical users. Thus, some CT manufacturers choose to set negative fat mass density values to zero.

3.F.3. Electron or mass density and effective atomic number images

The relationship between electron density (ρ^e) and mass density (ρ) is defined as

$$\rho^e = \frac{\rho}{A_m} Z N_A,$$

where Z is the atomic number, A_m is the atom mass, and N_A is Avogadro's number.

Effective atomic number (Z_{eff}) is defined as

$$Z_{eff} = \sum_i w_i^e Z_i^n, \quad i = 1, N \tag{13}$$

where w_i^e is the fraction of the total number of electrons of the ith material, Z_i is the atomic number of the ith material, N is the total number of materials in the sample, and n is a constant, usually in the range 3–4 in the literature (n = 3.5 in this report).[20,21] Additional definitions of the effective atomic number from a combination of known materials exist in the literature. More information is available in reference.[22]

Using the result of Eq. (10), the mass density and the effective atomic number can be obtained by solving the equations,

$$\begin{cases} a_p = \frac{K_1 Z_{eff}}{A} Z_{eff}^n \\ a_c = \frac{K_2}{A} Z_{eff} \end{cases}, \tag{14}$$

where A is the atomic mass number of the material, and K_1 and K_2 are constants.[4]

Material decomposition is not the only path to obtain the effective atomic number. A common method in dual-energy CT uses the ratio of linear attenuation coefficients from the low- and high-energy CT images. This linear attenuation ratio (LAR) is a function of effective atomic number (Z_{eff}) and its

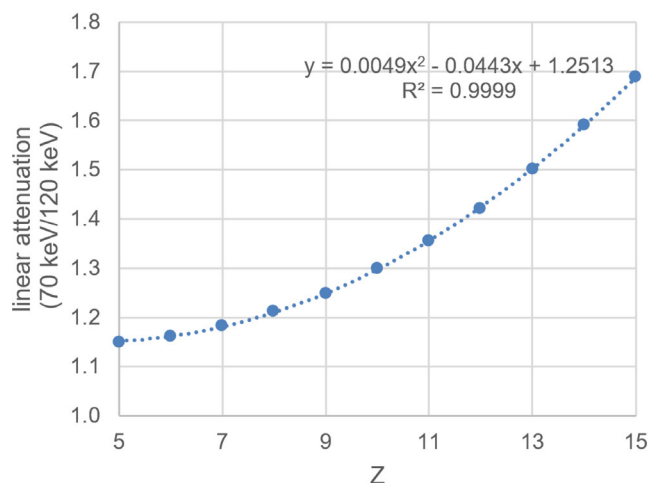FIG. 8. The data points represent linear attenuation ratio between 70 and 120 keV for the elements Z = 5–15. The dashed line and corresponding equation is the regression result, which can be used to determine the effective atomic number from the linear attenuation ratio of an unknown material, estimated from multienergy CT.

shape depends on the energy spectra of the images used in the calculation.

$$LAR(Z_{eff}) = \frac{\mu_L}{\mu_H}. \tag{15}$$

Usually LAR(Z_{eff}) is determined by calibration or simulation (Fig. 8), and then the LAR(Z_{eff}) curve is used as a lookup table for obtaining Z_{eff} of an unknown material.[12,21]

4. TECHNICAL IMPLEMENTATIONS OF MULTIENERGY CT

4.A. Detector-based methods

4.A.1. Dual-layer detectors

Description of technology: Acquisition of two spectrally distinct data sets can be achieved using a single x-ray source and two layers of energy-integrating scintillator detectors. The thickness and material of each layer determines the energy separation and relative noise of the recorded low- and high-energy datasets. In a commercially available system (IQon, Philips Healthcare, Cleveland, Ohio), the x-ray tube generates a polychromatic beam with a maximum photon energy equal to the peak tube potential selected by the user. Low-energy photons from the generated x-ray spectrum are selectively absorbed by the top low-density garnet scintillator layer, while high-energy photons pass through the top layer and are absorbed by the bottom G_2O_2S layer (Fig. 9).

Conventional CT data are also available from every scan by adding the low- and high-energy data together and reconstructing using standard techniques such as iterative reconstruction or filtered back-projection. The resulting images are conventional single-energy CT images, matching those obtained from
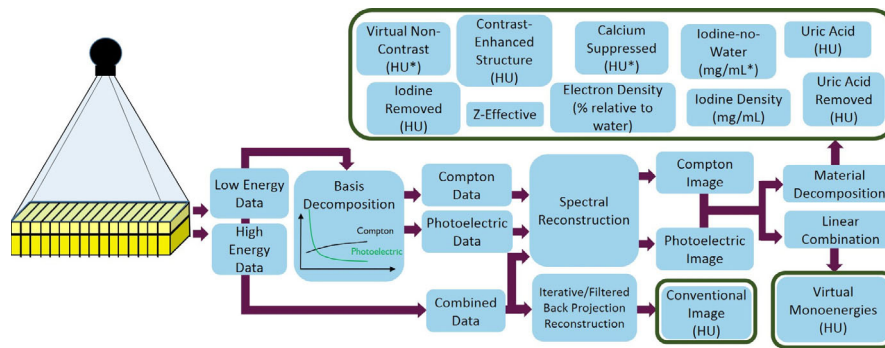
FIG. 9. Simultaneous acquisition of low and high energy x-ray spectra data allows projection-based spectral decomposition of the data into individual basis components with differing energy dependencies, specifically photoelectric effect and Compton scatter components. After decomposition, the data are reconstructed to obtain basis pair images. The photoelectric and Compton basis pair images can then be processed to obtain several types of spectral images, including both attenuation-based and nonattenuation based images. Low- and high-energy data can also be combined to create conventional (e.g., 120 kV) images. Asterisk (*) indicates that original pixel values may be modified significantly in some areas due to suppression of a particular material.

a conventional CT scanner operated with a single x-ray tube, single tube potential, and single-layer detector.

Ideally aligned low- and high-energy data are available from every scan performed at 120 or 140 kV. Intrinsic registration of spectral data allows projection domain decomposition. Reconstruction of basis pairs is performed with a dedicated spectral algorithm.[23–25] Material characterization and decomposition is performed using basis images to create various spectral image types (Fig. 9).

Strengths: One of the strengths of dual-layer detector technology is the absence of special protocols for dual-energy scanning. Routine scan protocols can be used "as is" without increasing dose or changing workflow. Both conventional and dual-energy data are available from every 120 and 140 kV scan and the need for dual-energy derived images does not have to be identified *a priori*. This can be particularly helpful for salvaging studies with suboptimal contrast enhancement, reducing artifacts on conventional images that obscure the region of interest, and improving lesion visualization and characterization, including incidentally discovered lesions. A study of 118 patients referred to dual-layer CT for a variety of clinical indications concluded that spectral information provided added clinical value in around 80% of scans, even though only 20% of scans would have been performed as a dual-energy acquisition based on clinical history and exam indication if an upfront choice had been required.[26]

Energy separation at the detector level yields low- and high-energy datasets that are spatially and temporally aligned, permitting projection space decomposition. A benefit of projection space decomposition is the intrinsic reduction in beam hardening artifacts. A reduction in beam hardening artifacts on virtual monoenergetic images created from dual-layer spectral CT data compared to conventional images has been demonstrated for head imaging,[25] myocardial perfusion imaging,[27] coronary stent imaging,[28] and imaging of hip prostheses.[29]

This registration of spectral data also allows the identification and removal of anti-correlated noise in basis material

raw data sets, facilitating noise suppression while preserving signal. Decreased noise in virtual monoenergetic images compared to conventional images created from the same data has been achieved using dual-layer technology.[28–31] Furthermore, several groups have reported nearly flat noise across the range of mono-energies evaluated (40 to 200 keV) and an increase in contrast-to-noise ratio (CNR) with decreasing keV.[28,30,31] Spatial and temporal registration of data sets also offers advantages for moving anatomy, such as the heart, when low- and high-energy information is combined to create spectral images. The dual-layer detector design also permits acquisition of dual-energy data at exactly the same phase of contrast enhancement.

Another strength of dual-layer detector technology is that it imposes no constraints on data acquisition related to field-of-view, gantry rotation time, or the utilization of dose saving tools such as tube current modulation. Additionally, the thickness and material of each detector layer can be chosen to provide low- and high-energy data with matching noise levels across typical patient sizes. This criterion is commonly used to balance the noise levels between the two data sets, as this provides a reasonable approach that is relatively robust for multiple applications. Moreover, the dual-layer solution is free from additional problems such as patient-induced cross scatter found in the dual-source approach and the reduction in spatial resolution due to the view interpolation required in the tube potential switching approach.

Limitations: The use of dual-layer detector technology with a single x-ray source has some limitations for dual energy CT. Because the energy separation of spectral data sets is limited by the fixed detector design, only scans performed at a tube potential of 120 or 140 kV may be used for spectral analysis. Routine scans can be performed at 80 or 100 kV, but only a conventional data set is available for reconstruction. The spectral separation with dual-layer detectors is worse than with approaches using two different tube potential settings and filtration of one of the beams, which in

principle will require a higher radiation dose to the patient to achieve an equivalent CNR in spectral images. This is somewhat mitigated by the removal of anti-correlated noise during material decomposition in projection space.

Another limitation of dual-layer detectors is the doubling of electronic noise since each reading is based on two channels of data. The detector design and operating parameters of the electronics help to minimize the impact of electronic noise. The electronic noise contribution typically remains below the quantum noise contribution such that the latter typically defines the limits of low dose scans. Finally, detector cross-talk between layers can occur, whereby photon interactions in one detector pixel result in scattered photons that interact in a different pixel.

4.A.2. Energy resolving, photon counting CT

Description of technology: Energy integration vs photon counting: The solid-state scintillation detectors used in today's medical CT systems convert x-rays into visible light, which is detected by photodiodes coupled to the scintillators. The intensity of the light produced per absorbed x-ray quantum and, as a consequence, the electrical signal produced per absorbed x-ray quantum, are proportional to the x-ray energy E. The signal S_{int} in the energy integration detector is the integral of the signal from all absorbed x-ray flux $N(E)$ over all energies E, with a weighting factor proportional to E.

$$S_{int} \approx \int_0^\infty E \cdot N(E) dE \qquad (16)$$

Solid-state scintillation detectors do not provide energy-resolved signals. Low-energy x-ray quanta, which carry most of the low-contrast information about an object, particularly iodine containing tissues, are therefore given less weight than are high-energy quanta in the integrated signal.

Photon-counting detectors based on semiconductors such as cadmium-telluride (CdTe) or cadmium-zinc-telluride (CZT) directly convert the x-rays into an electrical signal. The absorbed x-rays create electron-hole pairs that are separated in a strong electric field (voltage $\sim 10^6$ V/m) between the cathode and pixelated anode electrodes on top and at the bottom of the detector, respectively (Fig. 10). The moving electrons induce short voltage pulses, with pulse-heights approximately proportional to the x-ray energies E, which are individually counted as soon as they exceed a given energy threshold.

In a basic operation mode, with just one energy threshold E_1, all x-ray quanta above this threshold energy are counted with the same weight, resulting in a detector signal.

$$S_{count} \approx \int_{E_1}^\infty 1 \cdot N(E) dE \qquad (17)$$

The absence of the down-weighting of the signal from low-energy x-ray quanta can improve the CNR of the
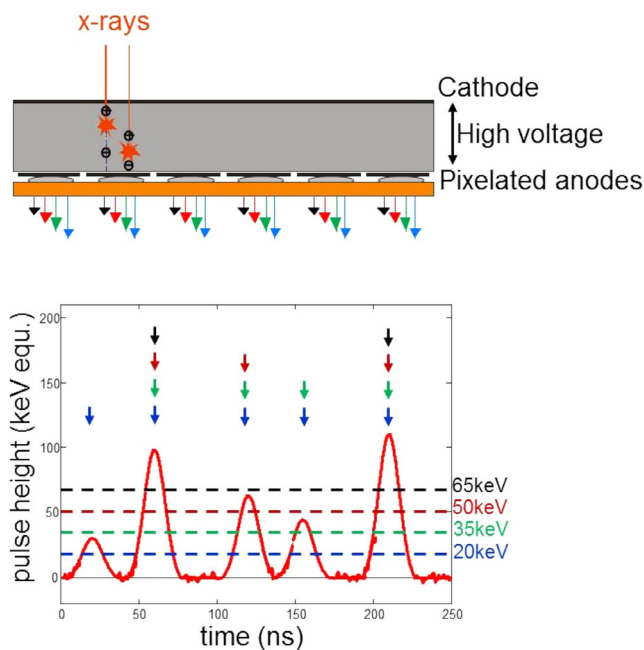

FIG. 10. Schematic drawing of a direct-converting photon counting detector (top). A semiconductor such as cadmium-telluride or cadmium-zinc-telluride absorbs the x-rays, which create electron-hole pairs that are separated in a strong electric field between the cathode and pixelated anodes. In this example, four energy thresholds are implemented for data read-out (20, 35, 50, and 65 keV). The x-ray photons are counted in the respective energy bins as soon as they exceed the corresponding energy thresholds (bottom).

resultant images, in particular in CT scans using an iodinated contrast agent.[32] Since only signals above the energy threshold are detected, low level electronic noise below the threshold does not affect the count rates in photon counting detectors. This is a major difference from conventional energy-integrating detectors, resulting in less image noise and the potential for dose reduction in scans of obese patients or in scans acquired at very low radiation dose.[33]

As illustrated in Fig. 10, different energy thresholds allow for the discrimination of photon energy. Photon counting detectors can simultaneously provide CT data with different lower energy thresholds E_1, E_2, to provide spectrally resolved measurements. Physically, the thresholds are realized by different voltages that are fed into pulse-height comparator circuits. The pulse heights obtained from the detector are nearly proportional to the energies of the detected x-ray photons. Up to six different threshold values have so far been used in prototype settings.

Strengths: By implementing two or more energy thresholds for data read-out, photon counting detectors can provide spectral (dual- or multienergy) data using standard CT scanners without modifications other than the detector type.[34] Spectral information is available in any scan, with no limitations in the choice of scan parameters such as tube potential, gantry rotation time or pitch, or in the use of anatomical tube current modulation to adapt the radiation dose to the patient's

anatomy. The inherent spatial and temporal alignment of the CT data at different energy levels benefits scans of moving organs, such as the heart, and enables the use of projection-based material decomposition. There is no additional scattered radiation that needs to be taken care of, such as the cross-scatter in dual source CT. With photon counting detectors, spectral data are routinely acquired, with the images at the lowest energy threshold used for standard diagnosis (similar to today's single energy CT images), and spectral information retrospectively available if clinically needed.

A technique refered to as K-edge imaging can be used to decompose materials into more than two basis materials (where one undergoes primarily Compton scattering interactions and the other undergoes primarily photoelectric interactions). Specifically, higher atomic number materials that have K-edges within the diagnostic CT energy range can be used as additional basis materials because their absoprtion edge discontinuities differentiate these materials from linear combinations of non-K-edge materials. Potential clinical applications include separation of iodine and gadolinium contrast agents after a multi-phasic injection to differentiate venous and arterial blood vessels,[35,36] separation of iodine, gadolinium, and bismuth to differentiate venous blood vessels, arterial bowel wall enhancement, and the contents of the bowel lumen,[37] or the separation of iodine and gold nano particles to evaluate oncologic and inflammatory diseases.[38]

Limitations: To date, photon counting detectors have only been available in research CT systems, which have been extensively evaluated from both the technical and clinical perspective.[32,39,40]

A main limitation of photon counting detectors today is the finite pulse-width of the detected x-ray pulses, which currently have a full-width-at-half-maximum (FWHM) of 10 ns and more. This leads to pulse pile-up at high x-ray flux values, as is common in medical CT. Pulse pile-up results in overlapping low-energy pulses being incorrectly registered as a fewer number of high-energy pulses, or several overlapping pulses being counted as only one pulse. As a consequence, photon counting detectors can saturate at high x-ray flux values, leading to significant quantum losses and increased image noise.

Another problem is count-rate drift. Nonhomogeneously distributed crystal defects in the sensor material can cause trapping of electrons and holes, a build-up of space charges, and a modification of the electric field distribution. This changes the characteristics of the signal pulses in the individual detector elements and may lead to severe ring artifacts in images at higher flux values. Significant progress has been made in reducing count-rate drift to acceptable levels.[39]

The spectral separation of photon counting detectors is affected by unavoidable physical effects, such as signal splitting at pixel borders (charge sharing) or energy loss of the x-ray quanta due to K-escape. K-escape occurs due to preferential absorption of photon energies near the K-edge(s) of the detector material and the consequential release of

characteristic x-rays. Charge sharing and K-escape events lead to a double counting of x-ray quanta at the wrong energies and therefore to a reduction in spectral separation.[41]

4.B. Source-based methods

4.B.1. Consecutive volume or helical acquisitions with different tube potentials per rotation

Description of technology: Wide-volume dual-energy imaging using two consecutive acquisitions takes advantage of the extended z-axis coverage available in a single axial rotation with wide-area detectors, such as the 16-cm Aquilion ONE detector introduced by Toshiba Medical Systems in 2009. In standard imaging applications, a 16-cm detector provides isotropic volume coverage of entire organs or regions of interest in a single 0.275-sec gantry rotation. For dual-energy applications, full organ coverage using two gantry rotations at the same location, each at a different tube potential value, allows for projection space alignment and projection-data-based material decomposition. When longer scan lengths are required, two helical scans performed with the identical trajectory may also be used. The noise level of the low- and high-energy acquisitions are controlled independently by adjusting the tube current value when the tube potentials are switched.

Strengths: A strength of the wide-area detector, two consecutive rotations approach to dual-energy CT is alignment of the projection space data, provided that there is no patient motion between the two gantry rotations. In addition, this approach lets the user take advantage of the automatic exposure control (AEC) system to adapt the tube current according to patient attenuation. This allows the image noise level to be matched between the low- and high-energy data acquisitions. Finally, this approach has stable tube potential values over the duration of the acquisition.

Limitations: The main limitation of the two consecutive acquisition approach to dual energy is motion misregistration and temporal alignment, as it can take as long as 500 milliseconds to switch from one tube potential to another between acquisitions. This limits its use in patients who move between acquisitions, in anatomic regions that undergo significant movement between acquisitions, such as in cardiac applications, or for tissues with rapid changes in contrast concentrations.

4.B.2. Acquisitions with rapid tube potential switching

Description of technology: The collection of low- and high-energy data sets by rapidly switching the tube potential back and forth between the low and high settings is often
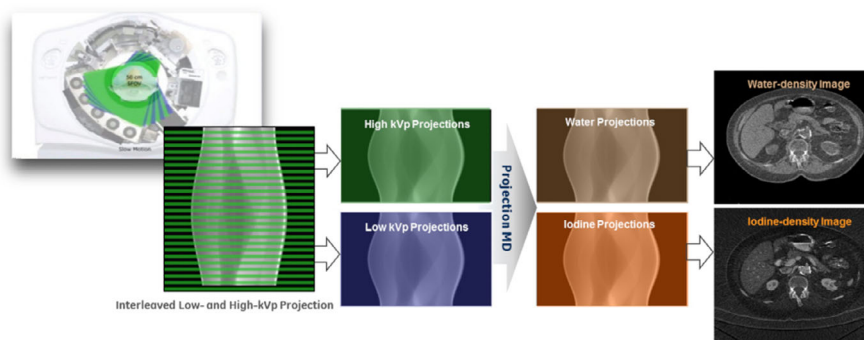
FIG. 11. Illustration of fast-kV switching, material decomposition and image reconstruction process.

referred to as fast-kV switching. The switching of the tube potential enables the acquisition of data from two different energy spectra that are closely aligned temporally and spatially.[42] The first commercial scanner for routine clinical imaging using fast-kV switching was introduced by GE Healthcare in 2008 (Discovery CT750 HD[TM]). In fast-kV switching, the x-ray tube potential is switched on a view to view basis. The acquired projection dataset is an interleaved sinogram, as shown in Fig. 11. Due to the temporal offset of the low- and high-energy projections, data interpolation is used to achieve data consistency between the low- and high-energy projections so that projection-space material decomposition can be performed. To maintain spatial resolution and reduce view-aliasing artifacts, the number of views collected per gantry rotation is more than doubled compared to a single tube potential scan. At a typical clinical rotation speed, the tube potentials, and therefore the output x-ray spectra, are changed within a fraction of a millisecond between 80 and 140 kV.

When more than two thousand views are collected per gantry rotation, the angular difference between adjacent 80- and 140-kV projections is smaller than 0.18°. This ensures that the neighboring views collected with different tube potentials correspond to the same patient anatomy viewed at nearly the same orientation. The adjacent views are also collected within a fraction of a millisecond to ensure that patient anatomy is minimally changed due to patient motion. These two properties allow the material decomposition to be carried out in the projection-space.[11,43]

The image generation process is as follows. The original interleaved 80- and 140-kV projections are sorted into two sinograms: 80 and 140 kV. Projection-space material decomposition is carried out and water (iodine)- and iodine (water)-density projections are generated. (On the GE system, the first material listed is the basis material being displayed and the material listed within the parenthesis is the other basis material used for the two-material decomposition). Tomographic reconstruction is then applied to these projections to produce water (iodine)- and iodine (water)-density images. Other images, such as virtual monoenergetic images, different basis-material pairs, or effective atomic number images can be calculated from the water and iodine pair. The entire process is pictorially depicted in Fig. 11.

The large change in the x-ray tube potential (60 kV) over a very short time places a significant technical demand on the CT system. First, the transition time between the low and high tube potential settings needs to be much shorter than the kV switching cycle in order to maintain sufficient energy separation. Slow rise- and fall-times induce signal contamination between the two tube potentials and lead to smaller energy difference between two sets of projections. A specially designed x-ray tube and generator are used to mitigate this reduction in spectral separation. This is important because adequate energy separation is essential for achieving good material decomposition and quantitation.[8]

Along with the fast tube potential switching times, the detector temporal response needs to be fast as well. All solid-state scintillators exhibit signal decay properties. If the decay speed is slow, signals generated from a previous projection will contaminate the current projection. Such contamination also leads to degraded energy separation. A specially engineered scintillator material, Gemstone[TM], is used to mitigate this effect.

The third technical challenge to fast-kV switching technology is x-ray flux management. Low-energy photons experience greater attenuation by the object than high-energy photons. However, for optimal noise performance, the noise present in the low- and high-energy measurements needs to be relatively balanced, since the material decomposition process depends on both measurements as inputs. To achieve this, fast-kV switching systems employ an asymmetrical sampling scheme in which the signal integration time for the low-energy projections is longer than the signal integration time for the high-energy projections.

It is important to note that tube-potential switching technology was commercially implemented in the 1980s. Because of the limitations of the technology available at that time, the tube current for the low-tube-potential data acquisitions could not be increased fast enough to achieve sufficiently low noise, which limited the system's use primarily to bone densitometry.[15]

Strengths: Since projection-space material decomposition is used in fast-kV switching, beam-hardening induced artifacts can be significantly reduced, which is important for

accurate dual-energy material quantitation. Furthermore, the fast-kV switching technique results in nearly simultaneous acquisition of the low- and high-energy projections, ensuring that motion-related issues are minimized. Since both sets of projections are acquired with the same detector used for routine CT imaging, the entire 50 cm field-of-view is covered (this is true for any detector-based methods if the detector(s) cover a 50 cm field-of-view). Finally, the ability to independently adjust the measured low- and high-energy flux based on the integration time for each energy's projections enables optimization of the system noise performance by taking into consideration the difference in patient attenuation characteristics between the two tube potentials.

Limitations: In the current commercial implementation of the fast-kV switching, the x-ray tube current cannot be changed dynamically during data acquisition. Hence, tube current modulation is not possible, which decreases the dose efficiency of the examination and limits the ability of the system to adapt to regions of increased patient attenuation. However, this is mainly due to hardware limitations on the existing system and is not a fundamental limitation of the fast-kV switching technology.

Both the finite switching time between the low and high tube potential settings and the finite detector temporal response introduce signal contamination between the low- and high-energy measurements, which reduces the accuracy of material quantitation and increases noise in images based on material decomposition. This contamination worsens as gantry rotation time is decreased, so the system software currently prevents the use of gantry rotation times of less than approximately 500 ms, which may limit the quality of cardiac examinations.

Additionally, because a single x-ray tube is used to collect all projection data and only a very short time exists between the acquisition of the low and high energy projections, further optimization of spectral separation by adding prefiltration to the high-energy beam would be difficult to achieve in practice, as it would require a system to move the filter into and out of the beam at extremely high rates and in a manner that was perfectly synchronized with the kV switching. Therefore, the energy separation for kV switching is worse than that of the dual-source approach, which allows the use of different beam filtration for the x-ray tube operating at the lower tube potential and the x-ray tube operating at the higher tube potential.

4.B.3. Beam filtration techniques

Description of technology: In 1980, a simple technique for obtaining dual-energy information from a standard CT acquisition was described.[44] The authors proposed to filter the two halves of the x-ray fan beam differently and use a 360° scan to obtain complete projection data for both spectra. This method has been implemented in a commercial CT-scanner (SOMATOM Edge and SOMATOM go. All, Siemens Healthcare GmbH, Forchheim, Germany). The x-ray

beam, however, is now split in the longitudinal direction and not in the fan beam direction. This is possible because of the multirow detector geometry, which was not available in 1980. Two different prefilters in the tube collimator housing are used to split the beam (Fig. 12). One half of the multirow detector in the scan direction sees an x-ray beam filtered with 0.6 mm tin; compared to the standard 120 kV spectrum, the mean energy of this prefiltered spectrum is increased. The other half of the detector sees an x-ray beam filtered with a thin gold filter; as a consequence of the K-edge of gold at 80.7 keV, the mean energy of this spectrum is decreased with respect to a conventional 120 kV spectrum. The total attenuation of the prefilters is adjusted to balance the radiation dose of the low- and high-energy portions of the beam.

The CT system may be operated in a spiral (helical) scan mode with a gantry rotation time as fast as 0.28 s and with pitch values up to 0.5 (referring to the full z-width of the detector). In this manner, each half of the detector along the z axis acquires a complete spiral dataset, and both low- and high-energy images can be reconstructed at any z-position as an input into image-based material decomposition techniques.

Strengths: Beam filtration techniques enable dual-energy scans with standard CT systems, with only small modifications of the tube collimator. No special tube or generator requirements are necessary. The dual-energy information is obtained over the full 50 cm diameter scan field of view and the radiation dose to the patient can be optimized by means of anatomical tube current modulation. A mixed image (a weighted average of low- and high-energy images that simulates a standard 120-kV image) dataset is the primary output of the acquisition. This enables routine dual-energy CT scanning while providing data similar to conventional imaging protocols. Compared with single-energy CT, similar image noise in the mixed images was demonstrated at 17% lower radiation dose.[45]
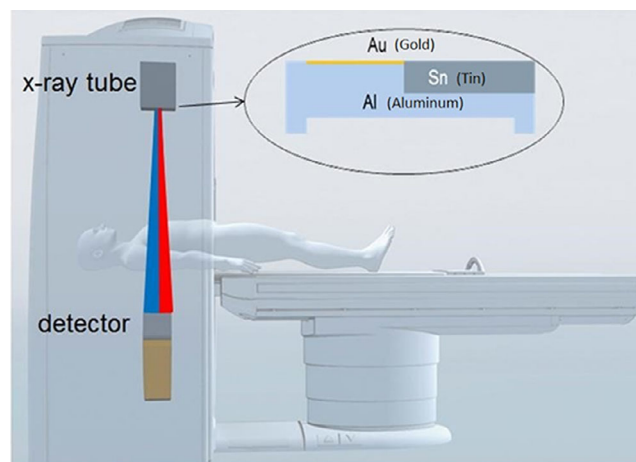

Fig. 12. Principle of a dual-energy computed tomography acquisition technique that uses a beam filter in the tube collimator housing to split the x-ray beam in the longitudinal direction.
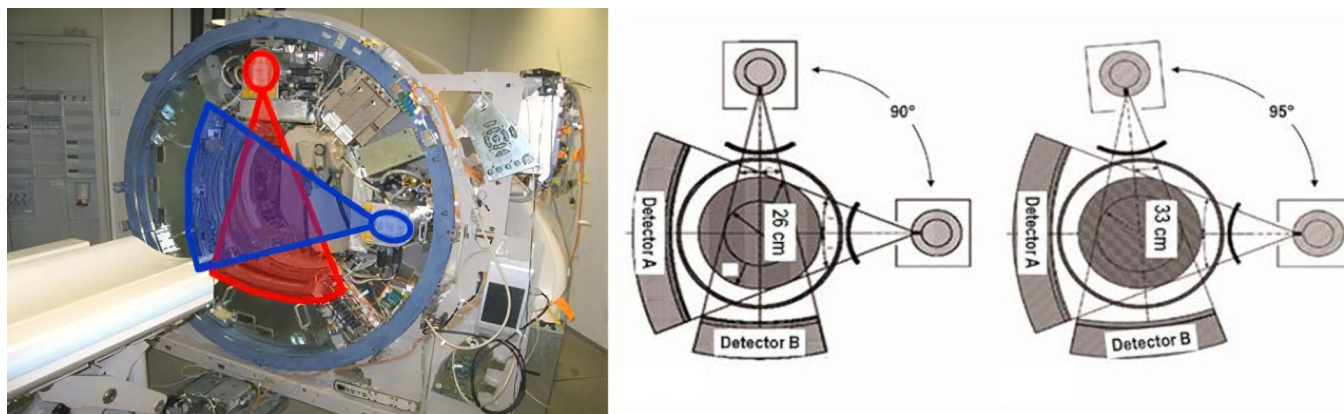
FIG. 13. Open gantry of a 1st generation dual source computed tomography (CT) (left). Schematic drawing of the tube-detector configuration of a 1st generation dual-source CT (DSCT) (center) and a 2nd generation DSCT (right), which has an increased scan field of view for detector B (right).

Limitations: The spectral separation with beam filtration techniques is not as good as when two different tube potential settings are used. Furthermore, a powerful x-ray tube is required because the prefiltration absorbs a significant portion of the x-ray flux, in turn limiting the use of this technique to nonobese patients. The maximum spiral pitch of 0.5 somewhat limits maximum volume coverage speed, albeit the use of 0.28 or 0.3 s rotation times can usually compensate for this limitation. Finally, scattered photons from the low-energy spectrum can be detected and counted as originating from the high-energy spectrum, and vice-versa.

4.B.4. Dual-source acquisitions

A dual-source CT (DSCT) is a CT system with two measurements systems, i.e., two x-ray tubes and two corresponding detectors, offset within the gantry at an angle of about 90°. Both measurement systems acquire scan data simultaneously at the same anatomical level of the patient (same z-position) (Fig. 13).[46] Dual energy data can be acquired by simultaneously operating both x-ray tubes at different tube potential settings, for example, 80 and 140 kV.[46,47]

In 2006, the first DSCT was commercially introduced (SOMATOM Definition, Siemens Healthcare GmbH, Forchheim, Germany). Its two acquisition systems, A and B, were mounted onto the rotating gantry with an angular offset of exactly 90°,[46] this was changed to an angular offset of 95° for the 2nd and 3rd generation DSCT systems (Fig. 13). Detector A covers the full scan field of view of 50 cm diameter, while detector B is restricted to a smaller field of view of 26 cm (1st generation), 33 cm (2nd generation), or 35.6 cm (3rd generation), as a consequence of space limitations on the gantry.

Strengths: With DSCT systems, the scan parameters (e.g., tube current and potential) can be individually adjusted for both measurement systems, resulting in a balanced radiation dose distribution between the low- and the high-energy scans. A wide range of routine scan protocols is available, with no restrictions in the choice of scan parameters such as gantry rotation time. Use of anatomical tube current modulation allows adaptation of the radiation dose to the patient's anatomy. Mixed images (a weighted average of low- and high-energy images) are routinely available, allowing dual-energy CT scans to be performed in routine clinical practice similar to conventional imaging protocols, with dual-energy information available when needed.

DSCT systems have the further ability to optimize spectral separation by introducing additional prefiltration into the high-energy beam, e.g., by means of a filter that can be moved into the beam when needed and moved out for nondual-energy applications. Dual-energy CT image quality and quantitative accuracy increases with better separation of the energy spectra. Energy separation results in increased image noise in basis-material decomposition, which has to be compensated for by increased radiation dose.[8,14,48,49] The 2nd generation DSCT is equipped with a 0.4 mm thick tin (Sn) filter to shift the mean energy of the 140 kV spectrum from 86 to 97 keV (after 20 cm water), as illustrated in Fig. 14. The mean energy of the 80 kV spectrum is 60 keV. The 3rd generation DSCT provides a 150 kV x-ray tube potential with more aggressive tin prefiltration (0.6 mm) to shift the mean energy of the 150 kV spectrum to 107 keV (Fig. 14). As additional benefits, the tin filter narrows the high energy spectrum, resulting in better dose efficiency and less beam hardening artifacts.

CTR can be used to quantify the performance of a dual-energy CT acquisition technique with regard to energy separation and material differentiation capability. The CTR for iodine, a commonly used basis material for material decomposition in contrast-enhanced CT scans, increases from ~2 using the 80/140 kV x-ray tube potential combination to ~3.4 using the 80/150 kV with 0.6 mm tin prefiltration x-ray tube potential combination (measured using a 20 cm water phantom[48]). A larger CTR value results in better-conditioned equations for basis-material differentiation and leads to less image noise in the material-specific images.[8,14,48] Alternative metrics to indicate the material differentiation capability of a
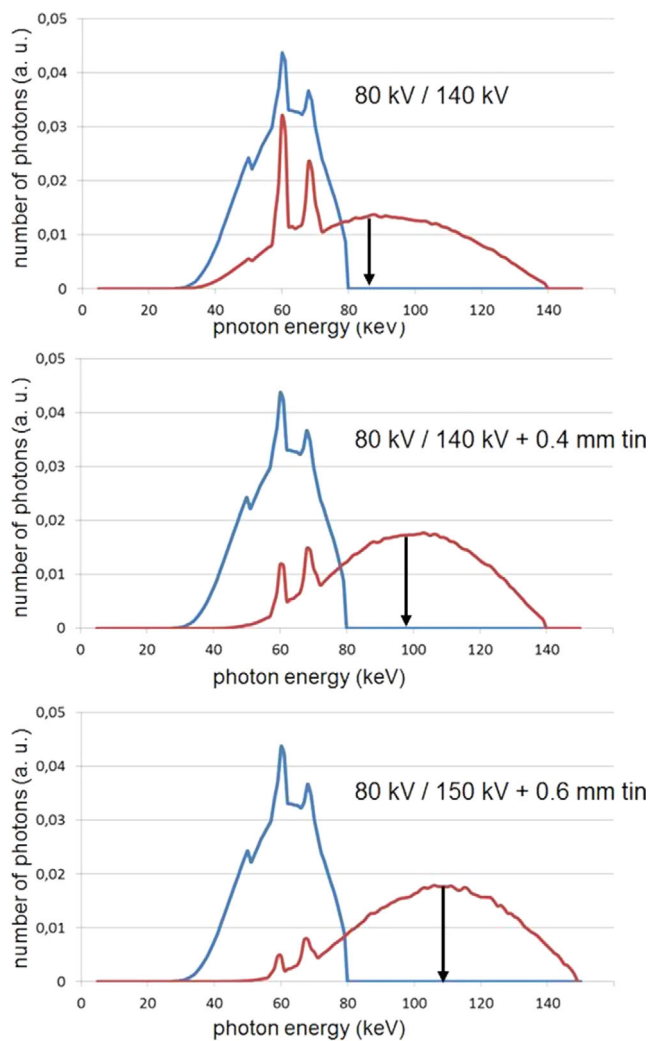
FIG. 14. Typical 80 and 140 kV spectra (after 20 cm water), normalized to equal areas under the curves (top). 80 kV spectrum and 140 kV spectrum with additional 0.4 mm tin prefiltration (center), and 80 kV spectrum and 150 kV spectrum with additional 0.6 mm tin prefiltration (bottom). Note the shift of the mean energy of the high energy spectrum to higher values (arrow) and the reduced spectral overlap.

dual-energy CT system include dual-energy index (DEI), dual-energy ratio (DER), and LAR, some of which take into account the effect of the background material, can be found in the literature.[8,13,14]

Limitations: Dual-energy evaluations with DSCT are restricted to the smaller central scan field of view of the smaller detector B. Mixed images, however, are obtained over the full 50 cm scan field of view.

Projection-based dual energy algorithms cannot be used with DSCT because the low- and high-energy projections are not simultaneously acquired at the same z-position. Dual energy algorithms are therefore image based. While there exists a theoretical advantage to projection-based algorithm, image-based methods have been shown to be practically

equivalent for certain clinical tasks. One prerequisite is the validity of the thin absorber model. With water and iodine as basis materials, the maximum x-ray attenuation of the iodine along any measured ray path must be small enough to assume a linear contribution to the total attenuation. This holds for iodine samples with integrated attenuation up to ~5000 HU·cm in water and is violated only in clinical situations where extremely high local concentrations of iodine are present, such as in CT nephrographic[50] or cardiac studies. As a second pre-requisite, the CT number of water and the CT numbers of small iodine samples should be independent of their position within the scanned object. To create these conditions, DSCT scanners are equipped with optimized bowtie filters to obtain adequate beam hardening. The patient, however, must be centered within the scan field of view.

Finally, cross-scattered radiation, i.e., scattered radiation originating from tube A and detected by detector B, and vice versa, has to be carefully corrected for to avoid distortions of CT numbers by cupping or streaking artifacts. This can be done either by measurement of cross-scattered radiation or by model-based approaches.[51]

5. CLINICAL APPLICATIONS

5.A. Material differentiation

5.A.1. Uric acid urinary stone differentiation (vs non-uric acid urinary stones)

Knowledge of urinary stone composition is critical for treatment and prevention of recurrence. In particular, the ability to distinguish uric acid ($C_5H_4N_4O_3$, $Z_{eff} \approx 6.9$) and non-uric acid stones is paramount.[52] The classification of stones based on the change of material attenuation values at low and high energies was one of the first clinical tasks explored with dual energy CT.[52–55] Evidence mounted as dual-energy technologies improved, and investigators evaluated approaches to not only differentiate uric acid and non-uric acid stones, but also to further differentiate different types of non-uric acid stones, as cystine ($C_6H_{12}N_2O_4S_2$, $Z_{eff} \approx 11.1$), calcium-based (includes oxalate $CaC_2O_4 \cdot H2O$, $Z_{eff} \approx 14.0$, brushite $CaHPO_4 \cdot 2H_2O$, $Z_{eff} \approx 14.2$, and struvite $CaMgNH_4 \cdot PO_4 \cdot 6H_2O$, $Z_{eff} \approx 12.6$), and apatite $Ca_{10}(PO_4)_6(OH)_2$, $Z_{eff} \approx 16.2$).[56,57]

Although multienergy CT has demonstrated improved accuracy in differentiating uric acid and non-uric acid stones and subclassifying non-uric acid stones compared with single energy CT, several limitations still exist.[58] First, the Z_{eff} values of non-uric acid stones fall within a very narrow range, from approximately 11 to 16, making it very difficult to separate these stone types because the Z_{eff} values are so similar. In contrast, the Z_{eff} value of uric acid (6.9) is very close to the Z_{eff} value of water (7.4). Hence, uric acid stones, though denser (brighter) than water, behave very differently in the dual-energy space than non-uric acid stones, which have Z_{eff} values well above that of water. This explains why the accuracy of separating uric acid from non-uric acid approaches
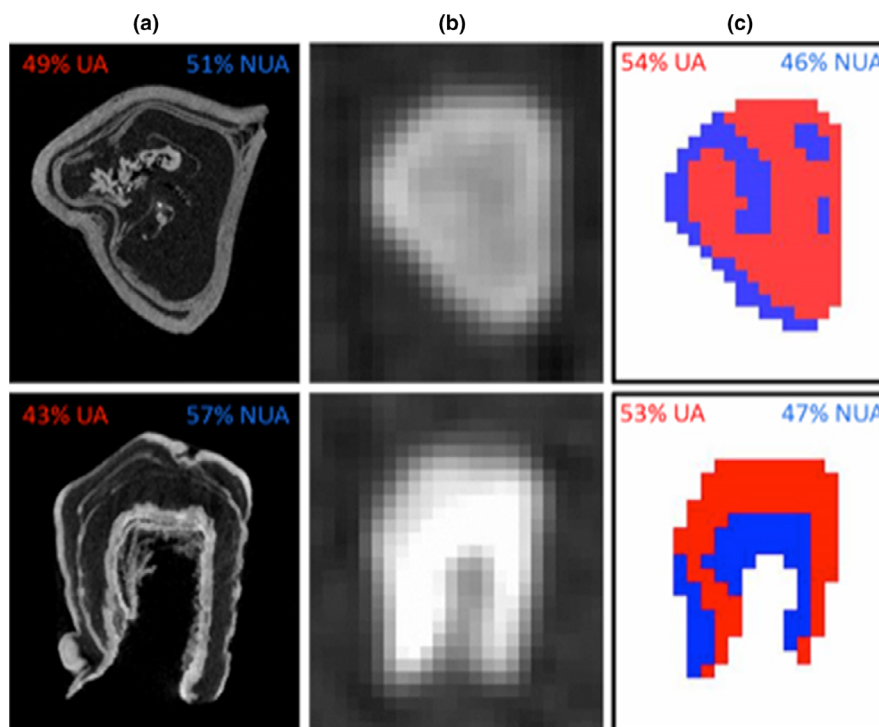
FIG. 15. Micro computed tomography (CT) images (column a, reference standard), dual-source CT images (column b), and color-coded dual-energy CT images (column c) identify uric-acid (UA, red) and non-uric acid (NUA, blue) components of these mixed stones. Best results were achieved by optimization of the cut-off CT number ratio used to separate the two categories. This cut-off value is, however, patient-size and scanner dependent. Machine learning approaches may address this limitation by "learning" these complex relationships in specimen and patient reference cases, and is an active area of research.[59] The clinical significance of the percentage composition values warrants further investigation.

100%, whereas to date, the separation of non-uric acid stone types has not been deemed sufficiently robust for clinical implementation.

Perhaps the most clinically significant limitation is the difficulty in correctly classifying stones with mixed uric acid and non-uric acid composition. This is due to limited spatial resolution, and hence partial volume averaging of the dual-energy attenuation values. Leng et al. varied the CTR threshold that separates uric acid from non-uric acid stone types and found that accurate quantification of uric acid and non-uric acid composition is possible with DSCT techniques in a study in which they compared DSCT data to micro-CT data of the same stones, demonstrating that identification of uric acid and non-uric acid mixed stones, and the relative contribution of each, is possible with dual-energy CT (Fig. 15).[59] Ongoing work in the field, including the determination of Z_{eff} with projection-based material decomposition, may address these limitations.[60]

5.A.2. Gout differentiation (vs pseudo-gout)

Gout and pseudo-gout are forms of arthritis that occur when crystals accumulate in the joints and periarticular soft tissues, including tendons and ligaments. Gout is characterized by uric acid crystals ($C_5H_4N_4O_3$, $Z_{eff} \approx 6.9$) and pseudo-gout by calcium pyrophosphate ($Ca_2O_7P_2$, $Z_{eff} \approx 15.6$) crystals. Treatment options differ such that

distinguishing between gout and pseudo-gout is clinically very important. The ability of multienergy CT to differentiate uric acid and calcium makes it well-suited for gout diagnosis (Fig. 16). Dual-energy attenuation differences are typically used to color-code the composition of tissue in the scanned region. Numerous studies have demonstrated good diagnostic accuracy of dual-energy CT for differentiating uric acid and calcium containing crystals in comparison to other available diagnostic imaging techniques such as ultrasound, digital radiography, and single energy CT.[61–63] A meta-analysis of multiple studies comparing dual-energy CT to standard diagnostic criteria, American College of Rheumatology criteria for classification of gout and/or monosodium urate crystal deposition, demonstrated high diagnostic accuracy of dual-energy CT for patients with gout.[64]

Studies support the usefulness of dual-energy CT not only for diagnosing gout but also for guiding treatment by monitoring the effectiveness of urate-lowering medical therapy. Dual-energy CT monitoring is enabled by its reproducible measurement of the number and volume of urate crystals.[65–67]

Limitations of dual-energy CT for evaluation and monitoring of gout have been noted and include lower sensitivity in patients with recent onset disease.[68,69] This may be associated with a failure to detect small, early urate crystals.[62] Additionally, artifacts arising from beam hardening or motion introduce the risk of a false positive diagnosis.[70]
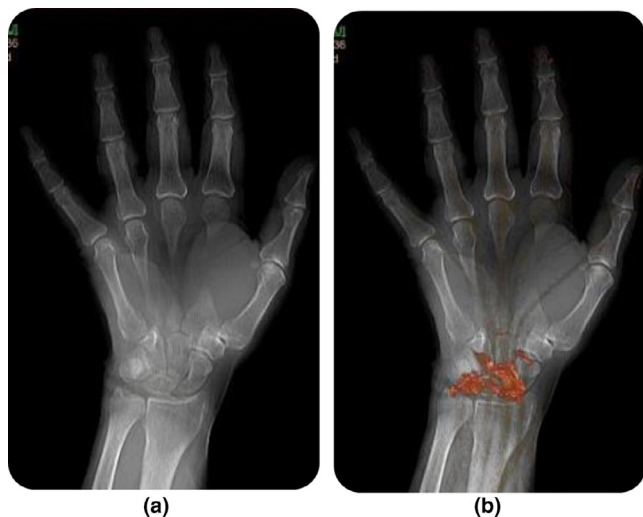
FIG. 16. Uric acid crystals characteristic of gout can be identified using dual energy computed tomography. Conventional image alone (a) and conventional image with uric acid overlay. (b) from a patient with confirmed gout. Multiple joint lesions are displayed in brownish-red in the overlay identifying them as uric acid crystals. Images courtesy of Hadassah Medical Center.

5.A.3. Silicone differentiation (vs dense soft tissue)

Silicone (one example formula $CH_3[Si(CH_3)_2O]_nSi(CH_3)_3$, $Z_{eff} \approx 10.7$) breast implants can rupture and leak into surrounding tissue. Attenuation differences between silicone and breast tissue are small and difficult to detect at single energy CT but the additional attenuation information available at multienergy CT allows visualization of the leak. Examples available in the literature clearly demonstrate the potential value of dual energy CT for evaluating the integrity of silicone breast implants (Fig. 17).[71–73]
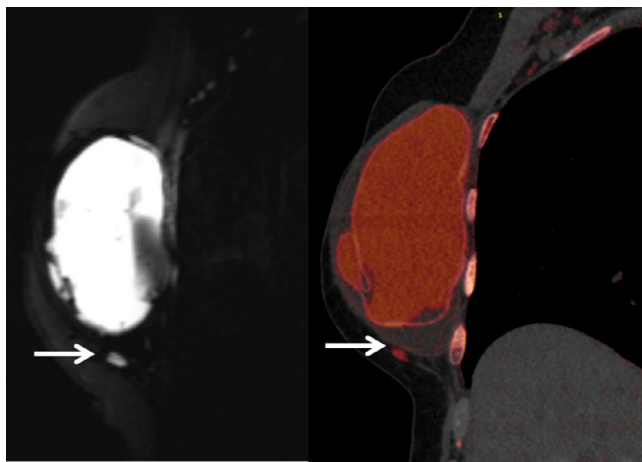

FIG. 17. Sixty-two-year-old woman with bilateral mastectomies and silicone implant reconstructions. Sagittal silicone-sensitive sequence magnetic resonance imaging (left) and sagittal dual-source, dual-energy computed tomography with silicone color coded in red (right) both demonstrate extracapsular silicone (arrows). Images courtesy of Mayo Clinic.

5.A.4. Bone differentiation (vs iodine)

Evaluation of contrast filled vessels on CT angiograms sometimes requires the removal of bone that can obscure the region of interest. Calcium and iodine are relatively easy to differentiate using dual energy attenuation values. This allows the identification and removal of bone on CT angiograms for direct visualization of contrast-enhanced vessels and organs. Dual-energy-based bone removal is considered useful for visualizing intracranial vessels[74–77] and identifying small or subtle intracranial abnormalities near bone (Fig. 18).[78] The utility for dual-energy CT bone removal in body imaging has also been demonstrated.[79–81]

Most studies to date have demonstrated improved image quality, fewer errors, and faster image review with automatic dual-energy bone removal compared to threshold-based single-energy techniques but limitations have also been noted. Clinically, dual-energy CT bone-removal is still vulnerable to some inaccuracies, for example due to image artifacts.[74] Also, for some dual energy CT technologies, beam hardening artifacts may actually be enhanced in bone-removed images.[76]

5.B. Material characterization

5.B.1. Creation of quantitative iodine and virtual non-contrast-enhanced maps

Dual-energy CT has been applied to help distinguish patients who have clear cell renal carcinoma from those who have papillary renal carcinoma.[82,83] These are the two main sub-types of renal cell cancer and they have quite different prognoses. They also have widely different treatment strategies, so correctly diagnosing this condition for individual patients is extremely important clinically (Fig. 19).

Several groups have applied dual-energy CT to this challenge. Mileto et al. utilized a DSCT system and measured the presence of iodine in renal lesions in 88 patients with pathologically confirmed disease.[82] A threshold of 0.9 mg/mL iodine allowed the discrimination of clear cell and papillary renal cell carcinoma. A similar study of 72 patients was undertaken using single-source fast kV- switching dual-energy CT[83]; for this technology and the same phase of contrast enhancement (nephrographic), the threshold for distinguishing these same two cell types was determined to be 1.28 mg/mL of iodine. This difference in threshold level between these two studies is likely due to many factors, including the dual-energy projection data separation, material decomposition approach, contrast enhancement timing, and patient population variability (differences in cardiac function for example). The relatively large difference in threshold values between these two studies (over 40%) points to the need for appropriate quality control, and for careful data handling procedures for patients examined using different multienergy CT technologies.

Dual-energy CT has also been successfully applied to distinguish hemorrhage from IV contrast staining and extravasation, first in a group of 18 patients,[84] then in a larger group of
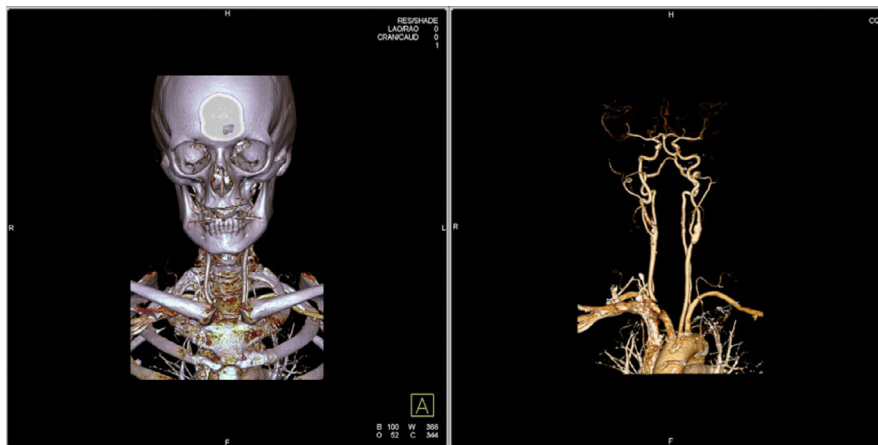
FIG. 18. Three-dimensional volume rendered images of a head and neck computed tomography (CT) angiogram prior to (left) and after (right) bone removal using dual-source, dual-energy CT. Images courtesy of Mayo Clinic.
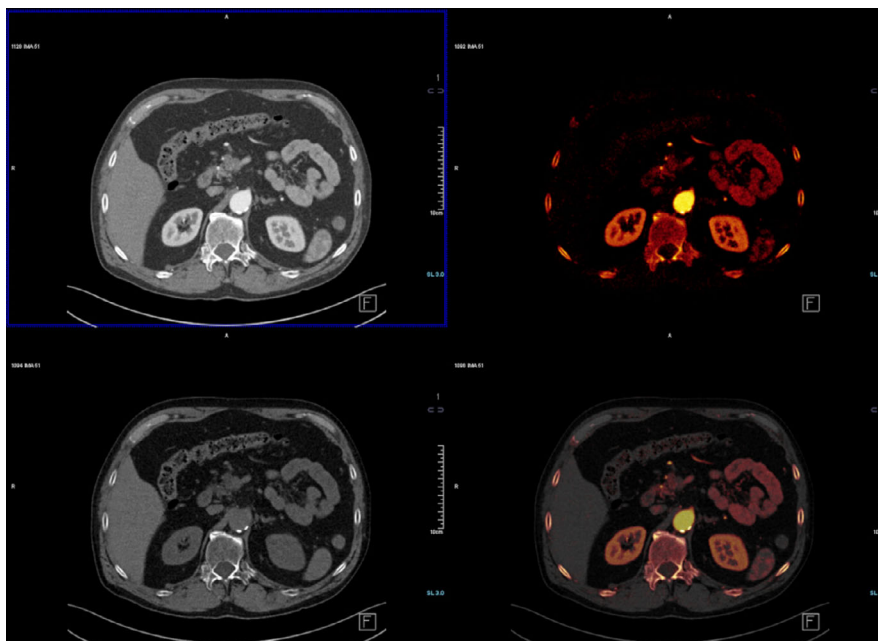
FIG. 19. Cross-sectional images at the level of the kidneys. Upper left: mixed image. Upper right: iodine map. Lower left: virtual non-contrast (VNC) image. Lower right: color iodine map overlaid on top of the grey-scale VNC image. Region of interest measurements yield computed tomography (CT) numbers for both the iodine and VNC images, as well as an estimate of iodine concentration in mg/ml. Images courtesy of Mayo Clinic.

40 patients in the context of stroke management.[85] The dual-energy approach has also been used to differentiate head and neck tumor bleeding from pure hemorrhage.[86] Promising work has been published regarding correlation of dual-energy CT measurements to thyroid nodule specimen pathologic results.[87] Many studies have examined the feasibility of replacing the separate noncontrast CT pass with a set of virtual unenhanced images, where the iodinated contrast material has been removed using the dual-energy CT analysis tool. One such relatively early publication showing the feasibility of this approach for brain imaging was published by Ferda et al.[88]

Many applications of multienergy CT have emerged for the abdomen/pelvis region. In addition to the renal carcinoma research described above, characterization of incidental findings[89] (eg renal cyst identification[90–92]) and evaluation of polycystic kidney disease[93] have benefitted from the application of dual-energy CT techniques. Detection and assessment of liver lesions is one of the more difficult challenges faced in CT; much work has been accomplished using dual-energy CT tools in this context.[94,95] Gastric cancer staging may also lend itself well to the utilization of dual-energy CT approaches.[96]
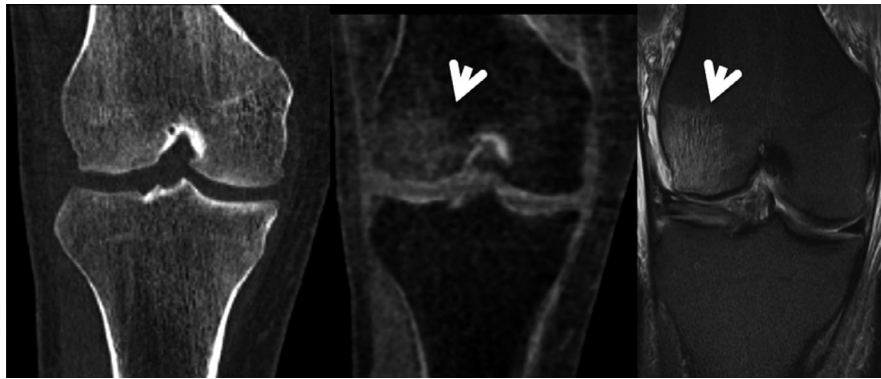
FIG. 20. Coronal images of a knee post traumatic injury. Left: conventional computed tomography (CT) image. Center: virtual noncalcium CT image. Right: Magnetic resonance image. The arrows point to the signal from edema in the bone, which is not visible in the presence of calcium in the conventional CT image. Images courtesy of Mayo Clinic.
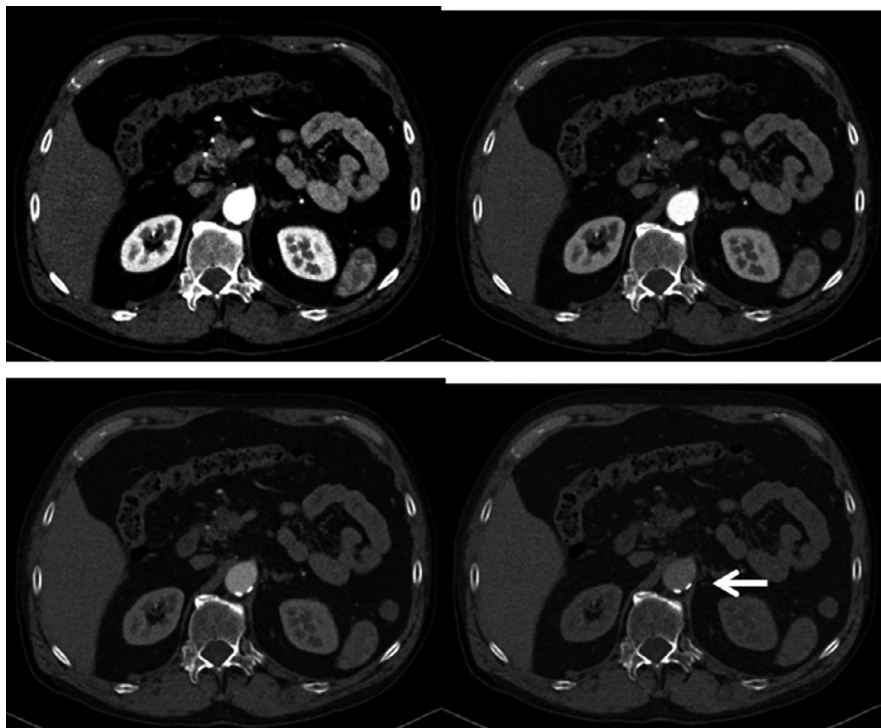
FIG. 21. Cross-sectional virtual monoenergetic images at the level of the kidneys (same case as in Fig. 19). Upper left: 50 keV. Upper right: 70 keV. Lower left: 100 keV. Lower right: 150 keV. The renal cortex and aorta are brightest at 50 keV and show very little enhancement at 150 keV, allowing the aortic calcifications (arrow) to be visualized. Images courtesy of Mayo Clinic.

5.B.2. Creation of quantitative calcium and virtual noncalcium maps

Sixty-two patients presenting in an emergency room setting were examined using dual-source dual-energy CT, using a three material decomposition model (brain parenchyma, hemorrhage, and calcium). Virtual noncalcium images and a calcium overlay were used to distinguish patients with a small hemorrhage from those with a small benign calcium deposit.[97] Similar approaches have been used to separate enhancing lesions from other highly attenuating physiologic structures.[98]

Characterization of pulmonary nodules is another potential application of multienergy CT measurement.[99–101] Other studies in the thoracic region have also provided promising results regarding dual-energy CT analysis.[102–106]

Another application of calcium-specific imaging is the ability to identify and remove calcium signal from bone. This allows visualization of bone marrow edema (ie "bone bruises"), which are otherwise not visible in conventional CT. This provides an alternative to MRI for the evaluation of bone bruises (Fig. 20).[107–109]
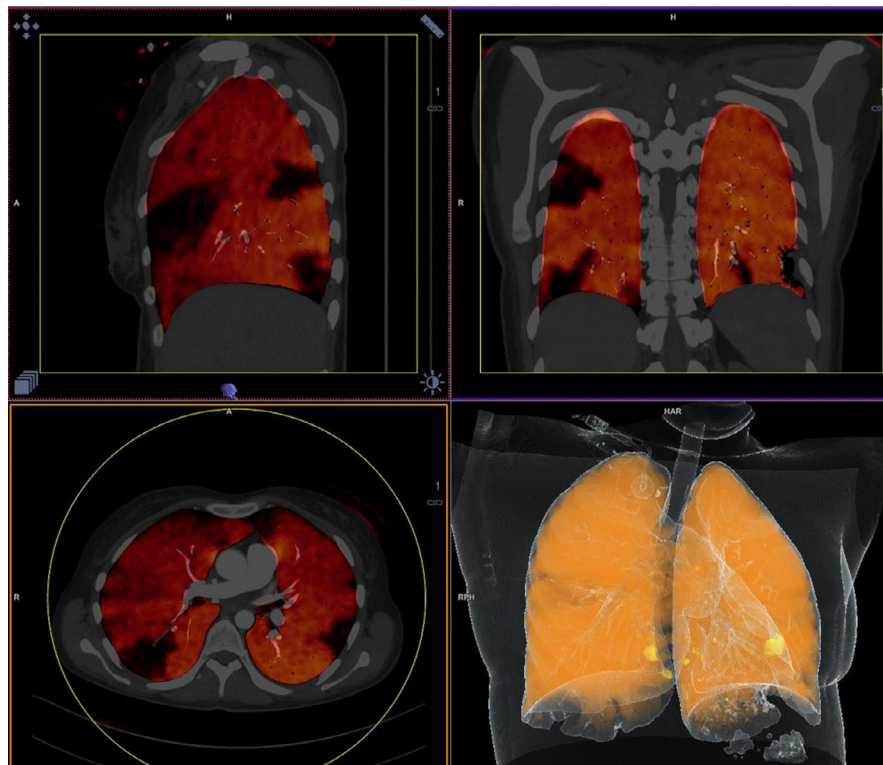
FIG. 22. Axial, sagittal and coronal perfused blood volume images demonstrate several large perfusion deficits. Iodinated blood is color-coded red (iodine map, HU). Black areas represent lung tissue with a perfusion deficit. Volume rendered images can be used to visualize the perfusion deficits in a 3-dimensional space. Images courtesy of Mayo Clinic.
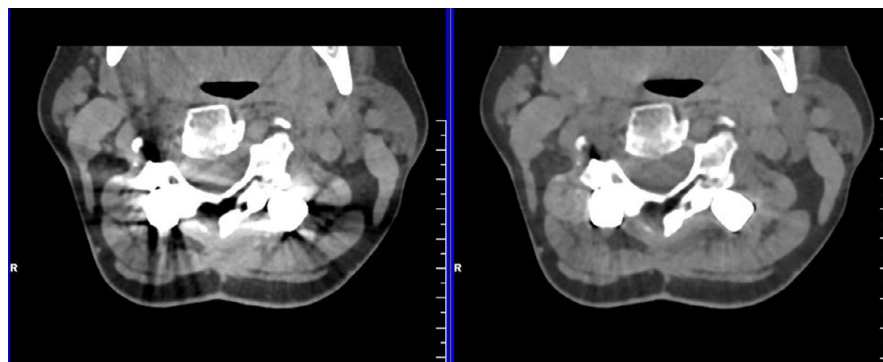
FIG. 23. Mixed (left) and 130 keV virtual monoenergetic (right) axial images of a cervical spine containing metal fixation rods. Images courtesy of Mayo Clinic.

5.B.3. Creation of quantitative virtual monoenergetic images

Much work has been accomplished to date regarding the optimal virtual monoenergetic energy levels to use for the head and neck region. Using a fast kV-switching dual-energy CT platform and 40 patients, the optimal virtual monoenergetic energy level for signal-to-noise-ratio measurements was found to be 65 keV, but the optimal virtual monoenergetic level for tumor conspicuity was the minimum level possible, 40 keV for this scanner.[110] Another study employing fast kV-switching dual-energy technology on 40 patients established that 40 and 70 keV were useful for identifying malignant from benign tissues, also in the head and neck region.[111]

Another study using the fast kV-switching dual-energy CT platform on 25 unenhanced head scans revealed that maximal grey matter signal-to-noise ratio, white matter signal-to-noise ratio, and grey matter to white matter contrast-to-noise ratio were obtained using 65 keV virtual monoenergetic images.[112] Optimal posterior fossa image quality was obtained at 75 keV. All of these measurements were found to be improved over the conventional (poly-energetic single-energy) image sets for these 25 patients.

Examination of 41 patients using a dual-source dual-energy CT approach focused on cerebral or cervical region vasculature determined that 60 keV virtual monoenergetic images resulted in optimal vessel attenuation and contrast-to-noise ratio.[113] A similar study focused on 71 patients with head and neck cancer determined that 60 keV virtual monoenergetic images provided the optimal lesion contrast-to-noise ratios and the highest subjective image quality scores. An example of virtual monoenergetic images of the abdomen at different keV settings is shown in Fig. 21.[114]

All of this work indicates that virtual monoenergetic images improve the usefulness of iodinated contrast and raises the question of the potential for reducing the volumes and/or concentrations of contrast material in the setting of dual-energy CT.[115] Multiple studies have been published which provide evidence that iodine contrast can be reduced by half in conjunction with the production with lower (40–60) keV monoenergetic images, without loss of visual enhancement. Multiphase liver CT and coronary CTA exams were both conducted with and directly compared to single energy CT images from the same patients, and found to be equivalent.[116,117] Additionally, results from patient and phantom studies performed on a dual-layer detector CT scanner indicated that the CNR of standard, polychromatic CT used for radiation oncology treatment planning in a pediatric population could be matched or improved on a 50 keV image acquired with administration of 50% less contrast.[118] Such a change would reduce the physiologic load on the kidneys for all patients, improving overall patient safety, and would presumably reduce the cost of contrast material for imaging facilities.

5.B.4. Creation of quantitative perfused blood volume images

Several publications have provided evidence that dual-energy CT imaging of the perfused blood volume in the lung can improve the detection of pulmonary embolus (Fig. 22). A perfused blood volume image, or map, usually superimposed on a gray-scale anatomic image, has been shown to improve the detection of peripheral intrapulmonary clots,[119] and to be useful for assessment of the severity of a perfusion deficit.[120,121] Perfused blood volume maps can be reported in terms of CT numbers (in HU) or in terms of absolute iodine concentration (in mg/mL), depending on the software provided by the manufacturer. A review of the use of dual energy CT for pulmonary diseases is given in reference.[122]

Dual-energy CT has also been used for perfused blood volume imaging of the myocardium during first-pass contrast enhancement. Dual-energy iodine maps are potentially more sensitive and more specific for the detection of hypo-perfused myocardium compared with hypo-attenuation on single-energy CT images.[123] ECG-controlled dual-energy CT has been performed at rest[124] and during pharmacologically induced stress[125] to detect both fixed perfusion defects and reversible ischemia. Alternatively, virtual monoenergetic images have been used in animal models to improve the quality of dynamic myocardial perfusion CT.[27] An overview of the uses of dual-energy CT for the assessment of myocardial perfusion can be found in the literature.[126,127]

5.B.5. Creation of electron density and effective atomic number images for radiation therapy applications

To exploit the potential benefits of proton therapy, accurate knowledge of the stopping power for the tissue traversed by the proton beam is necessary. Single-energy CT cannot discriminate between changes in patient density and chemical composition, which limits the accuracy of stopping power ratio (SPR) calculations. To overcome this limitation,[128–130] dual-energy CT has been used to calculate maps of the electron density relative to water $\rho_e/\rho_{e,w}$ and the effective atomic number Z_{eff} for a better prediction of SPR values, for example.[128,131] SPR calculation accuracy was found to be superior, on average, with dual-energy CT relative to single-energy CT.[132–134] Using the $\rho_e/\rho_{e,w}$ and Z_{eff} determined from dual-energy CT images, root-mean-square (RMS) errors as low as 0.2% are theoretically possible for human tissues.[128] In clinical practice, however, image noise reduces the accuracy of SPR calculations, as does nonidealities in the reconstructed images, such as beam-hardening and scatter.[135] Techniques that perform the material decomposition prior to image reconstruction have been investigated to address these limitations using sinogram data,[136] including using joint estimation methods.[137,138]

Another approach to improve SPR prediction and reduce CT-related uncertainties is the clinical use of virtual monoenergetic images,[139–141] which have improved CT number stability as patient size varies.[142] Furthermore, CT numbers from virtual monoenergetic images are accurate to within 10 HU across different CT scanner models from different CT scanner manufacturers.[143] These desirable properties reduce variations in the calculation of SPR values.

5.C. Artifact reduction

5.C.1. Beam hardening artifact reduction

As mentioned in the Introduction, CT systems use polychromatic x-ray beams which comprise photons across a spectrum of different energies that will experience varying, energy-dependent attenuation. At the detector level, the total transmitted intensity of the photon beam through the patient will represent the sum of the transmitted intensity at each energy comprising the beam. The assumption of a monoenergetic beam for reconstruction, particularly for long path lengths or high atomic number materials, can lead to beam hardening artifacts. Beam hardening correction algorithms based on the known attenuation characteristics of a single material, generally water, are reasonably effective at reducing artifacts for materials of similar atomic number to water. When the assumptions of the beam hardening correction algorithm are not met, the correction is often inadequate and artifacts can result, including shading and dark bands.

Multienergy CT can properly account for the polychromatic spectrum and allow for more robust beam-hardening correction through the generation of virtual monoenergetic images. Virtual monoenergetic images have shown promise with CT myocardial perfusion applications at reducing beam hardening artifacts, which can resemble myocardial perfusion defects, particularly in the posterobasal wall.[144] Similarly, another study found higher SNR and CNR values in the myocardium and coronary arteries using 60–80 keV monoenergetic images vs single-energy CT images.[145] Stolzmann found improvement in beam hardening artifact in 28/30 cases of dental restorations using virtual monoenergetic images vs single energy CT.[146]

5.C.2. Metal artifact reduction

Metal in the body represents a highly attenuating, high atomic number material that can confound the assumptions of conventional reconstruction algorithms, resulting in streaking, shading, and other artifacts. The artifacts associated with metal implants can have a variety of causes, but beam hardening is a significant cause of metal-related distortion. As such, virtual monoenergetic images can reduce metal artifacts.[115] Reduction or elimination of metal artifacts has been demonstrated for a large number of metallic objects, including hip arthroplasty/prosthesis, dental metallic implants, aortic repair stents, aneurysm clips, and more (Fig. 23).[29,147–153]

6. DOSIMETRIC CONSIDERATIONS

Similar to conventional single-energy CT, the multienergy CT acquisition and reconstruction parameters must be optimized for the imaging task while also considering the As Low As Reasonably Achievable (ALARA) principle. Provided that there is increased value in the material-specific information or increased iodine contrast-to-noise ratio, an increase in dose for multienergy CT with respect to single-energy CT is justified. However, the doses used in dual-energy CT are typically comparable to single-energy CT, if not lower, demonstrating that image quality can be maintained without a dose penalty.[58,154–157]

It is also important in multienergy CT to consider limitations of the technology being used. This is particularly important with regard to the low-energy dataset, as this is where noise is most prominent, artifacts are more likely to be induced, and quantification accuracy is most limited. Development of multienergy protocols therefore requires attention to the quality of the low-energy acquisitions, in addition to dosimetric considerations.

Tube current modulation is available on several commercially available multienergy CT systems. Masubara et al. compared image noise from 120 kV single-energy and dual-source, dual-energy CT acquisitions using custom-made elliptical polymethylmethacrylate phantoms of different sizes,[158] and empirically determined the optimal tube potential combinations and quality reference mAs values for different size phantoms. Similar work was performed by Michalak *et al.*, who determined the optimal tube potential combinations for dual-source, dual-energy virtual monoenergetic images.[159]

6.A. Review of published methods/doses

Conventional CT dosimetry techniques are well-established, although not without pitfalls. If such techniques were applied to the wide collimation on newer scanners without proper adaptation, a significant under reporting of the CT dose could be produced as a result of the limited length of the standard CT ionization chamber (100 mm) and broad dose profiles that extend beyond the length of the chamber.[160,161] A 60 cm long polyethylene phantom has been proposed by ICRU Report No. 87 and AAPM Report 200 to more accurately characterize broad dose profiles and minimize the dosimetry errors. Alternatively, AAPM Report 111 proposed to measure CT dose index ($CTDI_{100}$) free-in-air with no phantom present. The AAPM Report 111 method is applicable to helical and axial scanning modes; is valid for any beam width, table increment, and scan length; and can be applied to any shape phantom. In addition, an IEC standard has been established that all CT manufacturers must follow to appropriately report the dose for wide collimation scanners; this results in an approximately constant value of $CTDI_{vol}$ across all beam collimations.[162] This methodology mitigates the errors associated with the conventional CT dosimetry being applied to wide collimation scan modes.

Multienergy CT faces the same challenges as conventional CT when using an ionization chamber. Alternatively, there are commercially available radiation detection devices such as thermoluminescent dosimeters (TLD), optically stimulated luminescent dosimeters (OSL), and metal-oxide-semiconductor field-effect transistors (MOSFET). However, all of these devices have a known energy dependency that can be particularly problematic for multienergy CT. The potential use of these devices will require characterization of the different beam profiles at various energies and development of appropriate calibration factors.

CTDI-based dosimetry metrics quantify the radiation output of the CT scanner, which is important for standardization and performance assessment. However, it is often desirable to estimate the relative risk from a specific CT exam in comparison to other sources of ionizing radiation. The effective dose is a single parameter that accounts for biologic effects from a nonuniform, partial body exposure and can be used for these types of comparisons.

Two common methods used to determine effective dose from CT examinations are (a) Monte Carlo simulations that calculate organ-dose estimates and use tissue-weighting coefficients from the International Commission on Radiological Protection (ICRP),[163–166] and (b) a method that converts the dose-length product (DLP) to effective dose using published conversion coefficients.[167–171] Christner et al. investigated both methods for single-energy and dual-energy CT exams of the head, chest, coronary arteries, liver, abdomen, and

pelvis.[172] The investigators found no significant energy dependence with either method; the observed difference between single-energy and dual-energy effective dose calculations were within 8%.

Calculation of the effective dose from dual-energy CT chest exams has been performed by several additional authors.[173–175] Investigators used point dosimeters (TLD and MOSFET) and an anthropomorphic male phantom (Alderson Rando, The Phantom Laboratory, Salem, NY, USA), placing dosimeters into the phantom to obtain point measurements representative of the dose to specific organs; additional dosimeters were placed on the surface of the phantom to obtain entrance exposures. Paul et al. showed <0.4 mSv difference in effective doses between dual- and single-energy acquisitions using TLDs to measure organ doses in the chest and then calculating effective dose.[174] Mattison et al. developed a method to characterize the beam energy and calculate correction factors to address energy dependence to achieve an overall percent error of 5.9% when compared to the DLP method.[95] These studies, however, did not explicitly attempt to match image quality.

Schenzle et al. investigated radiation dose using TLDs and quantified noise and CNR for statistical evaluation of chest image quality. Measured effective doses were calculated to be 2.61, 2.69, and 2.70 mSv, respectively, for 80/140 kV, 100/Sn140 kV, and 120 kV single-energy acquisitions. Dual-energy images were created using a nonlinear blending algorithm. Resultant image noise values of 11.0, 10.7, and 9.9 HU ($P > 0.05$) and iodine CNR measurements of 33.4, 30.7, and 14.6 ($P < 0.05$) were measured for the 80/140 kV, 100/Sn140 kV, and 120 kV images, demonstrating that at the same radiation dose, image noise can be maintained and iodine CNR increased using dual-energy CT.

6.B. Changes in image quality due to noise reduction methods

Image noise in both single- and multienergy CT impacts detection of disease, contrast resolution, and quantification accuracy. Multienergy CT applications can be particularly susceptible to image noise due to the amplification of noise in the material decomposition process. Iterative reconstruction techniques have been applied to reduce the noise in the low- and high-energy images or the material-specific images. The general approach is to model the noise statistics or take advantage of noise correlations between the two source datasets to reduce image noise. The result is an ability to reduce radiation dose without increasing image noise. For low contrast objects, however, iterative reconstruction degrades edge sharpness, decreasing the overall ability to detect or resolve low contrast objects.[176,177]

Leng et al. have demonstrated that redundant information in the energy domain can be exploited to reduce noise (and hence dose) in multienergy CT.[178] A similar approach, using redundant information between the low- and high-energy images has been implemented by Bruder et al.[179] and Grant et al.[17] Bellini et al. investigated the noise improvement for

dual-energy CT exams of the pancreas using a commercially available version of these techniques and found that at all energies below 70 keV, noise was significantly decreased and CNR drastically increased.[180]

Petroongolo et al. developed an image-domain decomposition method for noise suppression in multienergy CT.[181] The method demonstrated an order of magnitude reduction in noise standard deviation while preserving high contrast spatial resolution, noise power spectra, and accuracy of electron density (<2% bias error), and the method was shown to be superior to filtering and iterative reconstruction.

6.C. Considerations for accurate quantification

Multienergy CT quantification requires the development of a quality control program to ensure accuracy and reproducibility. The methodology to quantify a particular element (i.e., iodine) or material (i.e., fat) varies between manufacturers, and includes utilizing known physical properties published by the National Institute of Standards and Technology (NIST) or user-defined parameter corrections for the material of interest. It is the responsibility of the user to ensure quantification accuracy and reproducibility; otherwise, significant caution is warranted regarding clinical conclusions and decisions.

The development of a quality control program often requires a phantom with known standards. There are currently several commercially available phantoms specifically designed to evaluate and monitor the quantitative accuracy of multienergy CT systems. A study by Nute et al. first reported on importance of a quality control program by demonstrating intrasystem variability and performance differences across dose levels.[182] The same group expanded the study by illustrating potential errors with respect to iodine quantification errors across multiple vendors. Jacobsen et al. identified systematic errors for iodine quantification when optimization of postprocessing parameters is not performed.[143]

Iodine quantification with multienergy CT has significant clinical importance as it is the predominant contrast material used clinically and offers tremendous opportunity to advance quantitative CT. Acquisition techniques (tube potential and beam filter combinations), reconstruction, and postprocessing can all have dramatic impact on quantitation, as exhibited by Krauss et al., where the iodine enhancement ratio increased with decreasing tube potential for the low-energy beam and increasing tube potential for the high-energy beam, especially when the tin filter was used for the high-energy beam.[39] Another important consideration with respect to quantitative CT is reproducibility from exam to exam, where variations in exams between different makes and models of scanners, and changes in patient size or table height can lead to erroneous results.[103,107]

The advantage with multienergy CT for iodine quantification relative to conventional CT has been reported to be an increased sensitivity when using material-specific decomposition or virtual monoenergetic imaging. This increase in sensitivity has led to an ability to reduce iodinated contrast

doses, which benefits patients with decreased renal function.[183]

Foley et al. discussed the importance of radiation dose on iodine sensitivity[183] and noted several studies that demonstrated a 25% increase in intrinsic iodine attenuation, and conversely a possible 25% reduction in iodine load, for dual-energy CT 70-keV monoenergetic images compared to 120 kV single energy CT images.[184–186] A number of investigators are developing and validating the accuracy and clinical utility of such techniques. Significant reductions in radiation dose, between 50% and 75%, have been demonstrated for the characterization of uric and non-uric acid stones with unenhanced dual-energy CT, while still maintaining the required sensitivity and specificity.[187,188] Besides iodine, there is strong clinical interest in quantification and characterization of other materials with multienergy CT.

7. SUMMARY

Dual-energy and multienergy CT techniques can differentiate materials of different effective atomic numbers, making possible new clinically relevant CT applications.[7] From approximately 2006–2009, applications were limited primarily to automated bone and plaque removal in CT angiography, removal of iodine signal from contrast-enhanced scans, single-phase imaging of perfused blood volume, and identification of tissues having specific elemental compositions. Since that time, additional applications have been developed and prospective clinical trials were performed to evaluate the clinical efficacy of these techniques.[7,189] The result is that dual- and multienergy CT is moving firmly into the mainstream of clinical CT imaging. Dual-energy CT may have disappeared from clinical consideration in the 1980s, but with the tremendous technical advances that have taken place since that time, modern CT technology is now capable of taking full advantage of the fundamental physics — and clinical promise — that Godfrey Hounsfield envisioned in 1973.

ACKNOWLEDGMENTS

a)Author to whom correspondence should be addressed. Electronic mail: mccollough.cynthia@mayo.edu.

REFERENCES

1. Hounsfield GN. Computerized transverse axial scanning (tomography). 1. Description of system. *Br J Radiol*. 1973;46:1016–1022.
2. International Commission on Radiation Units and Measurements. *Photon, Electron, Proton and Neutron Interaction Data for Body Tissues (Report 46)*. Bethesda, MD; 1992.
3. Hsieh J. *Computed Tomography: Principles, Design, Artifacts, and Recent Advances* (2nd Edition). Hoboken, NJ: John Wiley & Sons; 2015.
4. Alvarez RE, Macovski A. Energy-selective reconstructions in x-ray computerized tomography. *Phys Med Biol*. 1976;21:733–744.
5. Ergun DL, Mistretta CA, Brown DE, et al. Single-exposure dual-energy computed radiography: improved detection and processing. *Radiology*. 1990;174:243–249.
6. Kalender WA, Perman WH, Vetter JR, Klotz E. Evaluation of a prototype dual-energy computed tomographic apparatus. I. Phantom studies. *Med. Phys*. 1986;13:334–339.
7. McCollough CH, Leng S, Yu L, Fletcher JG. Dual- and multi-energy CT: principles, technical approaches, and clinical applications. *Radiology*. 2015;276:637–653.
8. Kelcz F, Joseph PM, Hilal SK. Noise considerations in dual energy CT scanning. *Med Phys*. 1979;6:418–425.
9. Williamson JF, Li S, Devic S, Whiting BR, Lerma FA. On two-parameter models of photon cross sections: application to dual-energy CT imaging. *Med Phys*. 2006;33:4115–4129.
10. Hubbell JH, Seltzer SM. Tables of X-Ray Mass Attenuation Coefficients and Mass Energy-Absorption Coefficients from 1 keV to 20 MeV for Elements Z = 1 to 92 and 48 Additional Substances of Dosimetric Interest (NISTIR 5632). U.S. Secretary of Commerce. https://www.nist.gov/pml/x-ray-mass-attenuation-coefficients. Published 1996. Accessed May 31, 2017.
11. Li B, Yadava G, Hsieh J. Quantification of head and body CTDIvol of dual-energy x-ray CT with fast-kVp switching. *Med Phys*. 2011;38:2595–2601.
12. Liu X, Yu L, Primak AN, McCollough CH. Quantitative imaging of element composition and mass fraction using dual-energy CT: three-material decomposition. *Med Phys*. 2009;36:1602–1609.
13. Mendonca PR, Lamb P, Sahani DV. A flexible method for multi-material decomposition of dual-energy CT images. *IEEE Trans Med Imaging*. 2014;33:99–116.
14. Primak AN, Ramirez Giraldo JC, Liu X, Yu L, McCollough CH. Improved dual-energy material discrimination for dual-source CT by means of additional spectral filtration. *Med Phys*. 2009;36:1359–1369.
15. Kalender WA, Klotz E, Kostaridou L. An algorithm for noise suppression in dual energy CT material density images. *IEEE Trans Med Imaging*. 1988;7:218–224.
16. Yu L, Christner JA, Leng S, Wang J, Fletcher JG, McCollough CH. Virtual monochromatic imaging in dual-source dual-energy CT: radiation dose and image quality. *Med Phys*. 2011;38:6371–6379.
17. Grant KL, Flohr TG, Krauss B, Sedlmair M, Thomas C, Schmidt B. Assessment of an advanced image-based technique to calculate virtual monoenergetic computed tomographic images from a dual-energy examination to improve contrast-to-noise ratio in examinations using iodinated contrast media. *Invest Radiol*. 2014;49:586–592.
18. Leng S, Yu L, Fletcher JG, McCollough CH. Maximizing iodine contrast-to-noise ratios in abdominal CT imaging through use of energy domain noise reduction and virtual monoenergetic dual-energy CT. *Radiology*. 2015;276:562–570.
19. Szczykutowicz TP. Hallway conversations in physics why do i see iodine signal coming from bones on dual-energy CT images? *Am J Roentgenol*. 2017;208:W193–W194.
20. Spiers FW. Effective atomic number and energy absorption in tissues. *Br J Radiol*. 1946;19:52–63.
21. Heismann B, Leppert J, Stierstorfer K. Density and atomic number measurements with spectral x-ray attenuation method. *J Appl Phys*. 2003;94:2073–2079.
22. Bonnin A, Duvauchelle P, Kaftandjian V, Ponard P. Concept of effective atomic number and effective mass density in dual-energy x-ray computed tomography. *Nucl Instrum Meth B*. 2014;318:223–231.
23. Ananthakrishnan L, Rajiah P, Ahn R, et al. Spectral detector CT-derived virtual non-contrast images: comparison of attenuation values with unenhanced CT. *Abdom Radiol*. 2017;42:702–709.

24. Pelgrim GJ, van Hamersvelt RW, Willemink MJ, et al. Accuracy of iodine quantification using dual energy CT in latest generation dual source and dual layer CT. *Eur Radiol*. 2017;27:3904–3912.

25. Neuhaus V, Abdullayev N, Hokamp N, et al. Improvement of image quality in unenhanced dual layer CT of the head using virtual monoenergetic images cmopared to polyenergetic single-energy CT. *Invest Radiol*. 2017;52:470–476.

26. Rajiah P, Rong R, Martinez-Rios C, Rassouli N, Landeras L. Benefit and clinical significance of retrospectively obtained spectral data with a novel detector-based spectral computed tomography – initial experiences and results. *Clin Imaging*. 2017;49:65–72.

27. Fahmi R, Eck BL, Levi J, et al. Quantitative myocardial perfusion imaging in a porcine ischemia model using a prototype spectral detector CT system. *Phys Med Biol*. 2016;61:2407–2431.

28. Hickethier T, Baessler B, Kroeger JR, et al. Monoenergetic reconstructions for imaging of coronary artery stents using spectral detector CT: in-vitro experience and comparison to conventional images. *J Cardiovasc Comput Tomogr*. 2017;11:33–39.

29. Wellenberg R, Boomsma M, Van Osch J, et al. Quantifying metal artefact reduction using virtual monochromatic dual-layer detector spectral CT imaging in unilateral and bilateral total hip protheses. *Eur J Radiol*. 2017;88:61–70.

30. Ehn S, Sellerer T, Muenzel D, et al. Assessment of quantification accuracy and image quality of a full-body dual-layer spectral CT system. *J Appl Clin Med Phys*. 2018;19:204–217.

31. Ozguner O, Dhanantwari A, Halliburton S, Wen G, Utrup S, Jordan D. Objective image characterization of a spectral CT scanner with dual-layer detector. *Phys Med Biol*. 2018;63:025027.

32. Gutjahr R, Halaweish AF, Yu Z, et al. Human imaging with photon counting-based computed tomography at clinical dose levels: contrast-to-noise ratio and cadaver studies. *Invest Radiol*. 2016;51:421–429.

33. Yu Z, Leng S, Kappler S, et al. Noise performance of low-dose CT: comparison between an energy integrating detector and a photon counting detector using a whole-body research photon counting CT scanner. *J Med Imaging (Bellingham)*. 2016;3:043503.

34. Si-Mohamed S, Bar-Ness D, Sigovan M, et al. Review of an initial experience with an experimental spectral photon-counting computed tomography system. *Nucl Instrum Methods Phys Res Sect A*. 2017;873:27–35.

35. Roessl E, Proksa R. K-edge imaging in x-ray computed tomography using multi-bin photon counting detectors. *Phys Med Biol*. 2007;52:4679–4696.

36. Muenzel D, Bar-Ness D, Roessl E, et al. Spectral photon-counting CT: initial experience with dual-contrast agent K-edge colonography. *Radiology*. 2017;283:723–728.

37. Symons R, Krauss B, Sahbaee P, et al. Photon-counting CT for simultaneous imaging of multiple contrast agents in the abdomen: an in vivo study. *Med Phys*. 2017;44:5120–5127.

38. Cormode DP, Si-Mohamed S, Bar-Ness D, et al. Multicolor spectral photon-counting computed tomography: in vivo dual contrast imaging with a high count rate scanner. *Sci Rep*. 2017;7:4784.

39. Kappler S, Hannemann T, Kraft E, et al. First results from a hybrid prototype CT scanner for exploring benefits of quantum-counting in clinical CT. *Proc SPIE*. 2012;8313:83130X.

40. Yu Z, Leng S, Jorgensen SM, et al. Evaluation of conventional imaging performance in a research whole-body CT system with a photon-counting detector array. *Phys Med Biol*. 2016;61:1572–1595.

41. Taguchi K, Iwanczyk JS. Vision 20/20: single photon counting x-ray detectors in medical imaging. *Med Phys*. 2013;40:100901.

42. Hsieh J, TU-E-, . 210A-01: dual-energy CT with fast-KVp switch. *Med Phys*. 2009;36;2749–2749.

43. Wu X, Langan DA, Xu D, et al. Monochromatic CT image representation via fast switching dual kVp. *Proc SPIE*. 2009;7258:725845.

44. Rutt B, Fenster A. Split-filter computed tomography: a simple technique for dual energy scanning. *J Comput Assist Tomogr*. 1980;4:501–509.

45. Euler A, Parakh A, Falkowski AL, et al. Initial results of a single-source dual-energy computed tomography technique using a split-filter: assessment of image quality, radiation dose, and accuracy of dual-energy applications in an in vitro and in vivo study. *Invest Radiol*. 2016;51:491–498.

46. Flohr TG, McCollough CH, Bruder H, et al. First performance evaluation of a dual-source CT (DSCT) system. *Eur Radiol*. 2006;16:256–268.

47. Johnson TR, Krauss B, Sedlmair M, et al. Material differentiation by dual energy CT: initial experience. *Eur Radiol*. 2007;17:1510–1517.

48. Krauss B, Grant KL, Schmidt BT, Flohr TG. The importance of spectral separation: an assessment of dual-energy spectral separation for quantitative ability and dose efficiency. *Invest Radiol*. 2015;50:114–118.

49. Primak AN, Giraldo JC, Eusemann CD, et al. Dual-source dual-energy CT with additional tin filtration: dose and image quality evaluation in phantoms and in vivo. *AJR Am J Roentgenol*. 2010;195:1164–1174.

50. Krauss B, Schmidt B, Flohr T. Dual Source CT. In: Johnson TR, ed. *Dual Energy CT in Clinical Practice*. Berlin: Springer-Verlag; 2011.

51. Petersilka M, Stierstorfer K, Bruder H, Flohr T. Strategies for scatter correction in dual source CT. *Med Phys*. 2010;37:5971–5992.

52. Primak AN, Fletcher JG, Vrtiska TJ, et al. Noninvasive differentiation of uric acid versus non-uric acid kidney stones using dual-energy CT. *Acad Radiol*. 2007;14:1441–1447.

53. Graser A, Johnson TR, Bader M, et al. Dual energy CT characterization of urinary calculi: initial in vitro and clinical experience. *Invest Radiol*. 2008;43:112–119.

54. Scheffel H, Stolzmann P, Frauenfelder T, et al. Dual-energy contrast-enhanced computed tomography for the detection of urinary stone disease. *Invest Radiol*. 2007;42:823–829.

55. Thomas C, Krauss B, Ketelsen D, et al. Differentiation of urinary calculi with dual energy CT: effect of spectral shaping by high energy tin filtration. *Invest Radiol*. 2010;45:393–398.

56. Eiber M, Holzapfel K, Frimberger M, et al. Targeted dual-energy single-source CT for characterisation of urinary calculi: experimental and clinical experience. *Eur Radiol*. 2012;22:251–258.

57. Qu M, Ramirez-Giraldo JC, Leng S, et al. Dual-energy dual-source CT with additional spectral filtration can improve the differentiation of non-uric acid renal stones: an ex vivo phantom study. *AJR Am J Roentgenol*. 2011;196:1279–1287.

58. Kaza RK, Ananthakrishnan L, Kambadakone A, Platt JF. Update of dual-Energy CT applications in the genitourinary tract. *AJR Am J Roentgenol*. 2017;208:1185–1192.

59. Leng S, Huang A, Cardona JM, Duan X, Williams JC, McCollough CH. Dual-energy CT for quantification of urinary stone composition in mixed stones: a phantom study. *AJR Am J Roentgenol*. 2016;207:321–329.

60. Kulkarni NM, Eisner BH, Pinho DF, Joshi MC, Kambadakone AR, Sahani DV. Determination of renal stone composition in phantom and patients using single-source dual-energy computed tomography. *J Comput Assist Tomogr*. 2013;37:37–45.

61. Bongartz T, Glazebrook KN, Kavros SJ, et al. Dual-energy CT for the diagnosis of gout: an accuracy and diagnostic yield study. *Ann Rheum Dis*. 2015;74:1072–1077.

62. Huppertz A, Hermann KG, Diekhoff T, Wagner M, Hamm B, Schmidt WA. Systemic staging for urate crystal deposits with dual-energy CT and ultrasound in patients with suspected gout. *Rheumatol Int*. 2014;34:763–771.

63. Kiefer T, Diekhoff T, Hermann S, et al. Single source dual-energy computed tomography in the diagnosis of gout: diagnostic reliability in comparison to digital radiography and conventional computed tomography of the feet. *Eur J Radiol*. 2016;85:1829–1834.

64. Lee YH, Song GG. Diagnostic accuracy of dual-energy computed tomography in patients with gout: a meta-analysis. *Semin Arthritis Rheum*. 2017;47:95–101.

65. Choi HK, Burns LC, Shojania K, et al. Dual energy CT in gout: a prospective validation study. *Ann Rheum Dis*. 2012;71:1466–1471.

66. Shi D, Xu JX, Wu HX, Wang Y, Zhou QJ, Yu RS. Methods of assessment of tophus and bone erosions in gout using dual-energy CT: reproducibility analysis. *Clin Rheumatol*. 2015;34:755–765.

67. Sun Y, Chen H, Zhang Z, et al. Dual-energy computed tomography for monitoring the effect of urate-lowering therapy in gouty arthritis. *Int J Rheum Dis*. 2015;18:880–885.

68. Jia E, Zhu J, Huang W, Chen X, Li J. Dual-energy computed tomography has limited diagnostic sensitivity for short-term gout. *Clin Rheumatol*. 2017;37:773–777.

69. Newberry SJ, FitzGerald JD, Motala A, et al. Diagnosis of gout: a systematic review in support of An American College of Physicians Clinical Practice Guideline. *Ann Intern Med.* 2017;166:27–36.

70. Coupal TM, Mallinson PI, Gershony SL, et al. Getting the most from your dual-energy scanner: recognizing, reducing, and eliminating artifacts. *AJR Am J Roentgenol.* 2016;206:119–128.

71. Glazebrook KN, Leng S, Jacobson SR, McCollough CM. Dual-energy CT for evaluation of intra- and extracapsular silicone implant rupture. *Case Rep Radiol.* 2016;2016:6323709.

72. Johnson TR, Himsl I, Hellerhoff K, et al. Dual-energy CT for the evaluation of silicone breast implants. *Eur Radiol.* 2013;23:991–996.

73. Glazebrook KN, Doerge S, Leng S, et al. Ability of dual-energy CT to detect silicone gel breast implant rupture and nodal silicone spread. *AJR Am J Roentgenol.* 2019;212:933–942.

74. Buerke B, Wittkamp G, Seifarth H, Heindel W, Kloska SP. Dual-energy CTA with bone removal for transcranial arteries: intraindividual comparison with standard CTA without bone removal and TOF-MRA. *Acad Radiol.* 2009;16:1348–1355.

75. Morhard D, Fink C, Graser A, Reiser MF, Becker C, Johnson TR. Cervical and cranial computed tomographic angiography with automated bone removal: dual energy computed tomography versus standard computed tomography. *Invest Radiol.* 2009;44:293–297.

76. Naruto N, Tannai H, Nishikawa K, et al. Dual-energy bone removal computed tomography (BRCT): preliminary report of efficacy of acute intracranial hemorrhage detection. *Emerg Radiol.* 2017;25:29–33.

77. Zhang LJ, Wu SY, Poon CS, et al. Automatic bone removal dual-energy CT angiography for the evaluation of intracranial aneurisms. *J Comput Assist Tomogr.* 2010;34:816–824.

78. Kuno H, Sekiya K, Chapman MN, Sakai O. Miscellaneous and emerging applications of dual-energy computed tomography for the evaluation of intracranial pathology. *Neuroimaging Clin N Am.* 2017;27:411–427.

79. Brockmann C, Jochum S, Sadick M, et al. Dual-energy CT angiography in peripheral arterial occlusive disease. *Cardiovasc Intervent Radiol.* 2009;32:630–637.

80. Schulz B, Kuehling K, Kromen W, et al. Automatic bone removal technique in whole-body dual-energy CT angiography: performance and image quality. *AJR Am J Roentgenol.* 2012;199:W646–W650.

81. Sommer WH, Johnson TR, Becker CR, et al. The value of dual-energy bone removal in maximum intensity projections of lower extremity computed tomography angiography. *Invest Radiol.* 2009;44:285–292.

82. Mileto A, Marin D, Alfaro-Cordoba M, et al. Iodine quantification to distinguish clear cell from papillary renal cell carcinoma at dual-energy multidetector CT: a multireader diagnostic performance study. *Radiology.* 2014;273:813–820.

83. Zarzour JG, Milner D, Valentin R, et al. Quantitative iodine content threshold for discrimination of renal cell carcinomas using rapid kV-switching dual-energy CT. *Abdominal radiology.* 2017;42:727–734.

84. Gupta R, Phan CM, Leidecker C, et al. Evaluation of dual-energy CT for differentiating intracerebral hemorrhage from iodinated contrast material staining. *Radiology.* 2010;257:205–211.

85. Phan CM, Yoo AJ, Hirsch JA, Nogueira RG, Gupta R. Differentiation of hemorrhage from iodinated contrast in different intracranial compartments using dual-energy head CT. *AJNR Am J Neuroradiol.* 2012;33:1088–1094.

86. Kim SJ, Lim HK, Lee HY, et al. Dual-energy CT in the evaluation of intracerebral hemorrhage of unknown origin: differentiation between tumor bleeding and pure hemorrhage. *AJNR Am J Neuroradiol.* 2012;33:865–872.

87. Li M, Zheng X, Li J, et al. Dual-energy computed tomography imaging of thyroid nodule specimens: comparison with pathologic findings. *Invest Radiol.* 2012;47:58–64.

88. Ferda J, Novak M, Mirka H, et al. The assessment of intracranial bleeding with virtual unenhanced imaging by means of dual-energy CT angiography. *Eur Radiol.* 2009;19:2518–2522.

89. Wortman JR, Bunch PM, Fulwadhva UP, Bonci GA, Sodickson AD. Dual-energy CT of incidental findings in the abdomen: can we reduce the need for follow-up imaging? *AJR Am J Roentgenol.* 2016;207: W58–W68.

90. Graser A, Johnson TR, Chandarana H, Macari M. Dual energy CT: preliminary observations and potential clinical applications in the abdomen. *Eur Radiol.* 2009;19:13–23.

91. Graser A, Johnson TR, Hecht EM, et al. Dual-energy CT in patients suspected of having renal masses: can virtual nonenhanced images replace true nonenhanced images? *Radiology.* 2009;252:433–440.

92. Graser A, Becker CR, Staehler M, et al. Single-phase dual-energy CT allows for characterization of renal masses as benign or malignant. *Invest Radiol.* 2010;45:399–405.

93. Arndt N, Staehler M, Siegert S, Reiser MF, Graser A. Dual energy CT in patients with polycystic kidney disease. *Eur Radiol.* 2012;22:2125–2129.

94. Mendler MH, Bouillet P, Le Sidaner A, et al. Dual-energy CT in the diagnosis and quantification of fatty liver: limited clinical value in comparison to ultrasound scan and single-energy CT, with special reference to iron overload. *J Hepatol.* 1998;28:785–794.

95. Raptopoulos V, Karellas A, Bernstein J, Reale FR, Constantinou C, Zawacki JK. Value of dual-energy CT in differentiating focal fatty infiltration of the liver from low-density masses. *AJR Am J Roentgenol.* 1991;157:721–725.

96. Pan Z, Pang L, Ding B, et al. Gastric cancer staging with dual energy spectral CT imaging. *PLoS ONE.* 2013;8:e53651.

97. Hu R, Daftari Besheli L, Young J, et al. Dual-energy head CT enables accurate distinction of intraparenchymal hemorrhage from calcification in emergency department patients. *Radiology.* 2016;280:177–183.

98. Vogl TJ, Schulz B, Bauer RW, Stover T, Sader R, Tawfik AM. Dual-energy CT applications in head and neck imaging. *AJR Am J Roentgenol.* 2012;199:S34–S39.

99. Chae EJ, Song JW, Krauss B, et al. Dual-energy computed tomography characterization of solitary pulmonary nodules. *J Thorac Imaging.* 2010;25:301–310.

100. Knoss N, Hoffmann B, Krauss B, Heller M, Biederer J. Dual energy computed tomography of lung nodules: differentiation of iodine and calcium in artificial pulmonary nodules in vitro. *Eur J Radiol.* 2011;80: e516–e519.

101. Chae EJ, Song JW, Seo JB, Krauss B, Jang YM, Song KS. Clinical utility of dual-energy CT in the evaluation of solitary pulmonary nodules: initial experience. *Radiology.* 2008;249:671–681.

102. Lee SH, Hur J, Kim YJ, Lee HJ, Hong YJ, Choi BW. Additional value of dual-energy CT to differentiate between benign and malignant mediastinal tumors: an initial experience. *Eur J Radiol.* 2013;82:2043–2049.

103. Schmid-Bindert G, Henzler T, Chu TQ, et al. Functional imaging of lung cancer using dual energy CT: how does iodine related attenuation correlate with standardized uptake value of 18FDG-PET-CT? *Eur Radiol.* 2012;22:93–103.

104. Kawai T, Shibamoto Y, Hara M, Arakawa T, Nagai K, Ohashi K. Can dual-energy CT evaluate contrast enhancement of ground-glass attenuation? Phantom and preliminary clinical studies. *Academic radiology.* 2011;18:682–689.

105. Chae EJ, Seo JB, Goo HW, et al. Xenon ventilation CT with a dual-energy technique of dual-source CT: initial experience. *Radiology.* 2008;248:615–624.

106. Thieme SF, Becker CR, Hacker M, Nikolaou K, Reiser MF, Johnson TR. Dual energy CT for the assessment of lung perfusion–correlation to scintigraphy. *Eur J Radiol.* 2008;68:369–374.

107. Ai S, Qu M, Glazebrook KN, et al. Use of dual-energy CT and virtual non-calcium techniques to evaluate post-traumatic bone bruises in knees in the subacute setting. *Skeletal Radiol.* 2014;43:1289–1295.

108. Pache G, Krauss B, Strohm P, et al. Dual-energy CT virtual noncalcium technique: detecting posttraumatic bone marrow lesions–feasibility study. *Radiology.* 2010;256:617–624.

109. Wang CK, Tsai JM, Chuang MT, Wang MT, Huang KY, Lin RM. Bone marrow edema in vertebral compression fractures: detection with dual-energy CT. *Radiology.* 2013;269:525–533.

110. Lam S, Gupta R, Levental M, Yu E, Curtin HD, Forghani R. Optimal virtual monochromatic images for evaluation of normal tissues and head and neck cancer using dual-energy CT. *AJNR Am J Neuroradiol.* 2015;36:1518–1524.

111. Yamauchi H, Buehler M, Goodsitt MM, Keshavarzi N, Srinivasan A. Dual-energy CT-based differentiation of benign posttreatment changes from primary or recurrent malignancy of the head and neck: comparison of spectral hounsfield units at 40 and 70 keV and iodine concentration. *AJR Am J Roentgenol.* 2016;206:580–587.

112. Pomerantz SR, Kamalian S, Zhang D, et al. Virtual monochromatic reconstruction of dual-energy unenhanced head CT at 65–75 keV maximizes image quality compared with conventional polychromatic CT. *Radiology*. 2013;266:318–325.

113. Schneider D, Apfaltrer P, Sudarski S, et al. Optimization of kiloelectron volt settings in cerebral and cervical dual-energy CT angiography determined with virtual monoenergetic imaging. *Acad Radiol*. 2014;21:431–436.

114. Wichmann JL, Noske EM, Kraft J, et al. Virtual monoenergetic dual-energy computed tomography: optimization of kiloelectron volt settings in head and neck cancer. *Invest Radiol*. 2014;49:735–741.

115. Albrecht MH, Vogl TJ, Martin SS, et al. Review of clinical applications for virtual monoenergetic dual-energy CT. *Radiology*. 2019;293:260–271.

116. Carrascosa P, Leipsic JA, Capunay C, et al. Monochromatic image reconstruction by dual energy imaging allows half iodine load computed tomography coronary angiography. *Eur J Radiol*. 2015;84:1915–1920.

117. Nagayama Y, Nakaura T, Oda S, et al. Dual-layer DECT for multiphasic hepatic CT with 50 percent iodine load: a matched-pair comparison with a 120 kVp protocol. *Eur Radiol*. 2017;28:1719–1730.

118. Tsang DS, Merchant TE, Merchant SE, Smith H, Yagil Y, Hua CH. Quantifying potential reduction in contrast dose with monoenergetic images synthesized from dual-layer detector spectral CT. *Br J Radiol*. 2017;90:20170290.

119. Okada M, Kunihiro Y, Nakashima Y, et al. Added value of lung perfused blood volume images using dual-energy CT for assessment of acute pulmonary embolism. *Eur J Radiol*. 2015;84:172–177.

120. Miura S, Ohno Y, Kimura H, Kichikawa K. Quantitative lung perfused blood volume imaging on dual-energy CT: capability for quantitative assessment of disease severity in patients with acute pulmonary thromboembolism. *Acta Radiol*. 2015;56:284–293.

121. Sakamoto A, Sakamoto I, Nagayama H, Koike H, Sueyoshi E, Uetani M. Quantification of lung perfusion blood volume with dual-energy CT: assessment of the severity of acute pulmonary thromboembolism. *AJR Am J Roentgenol*. 2014;203:287–291.

122. Kang MJ, Park CM, Lee CH, Goo JM, Lee HJ. Dual-energy CT: clinical applications in various pulmonary diseases. *Radiographics*. 2010;30:685–698.

123. Ruzsics B, Schwarz F, Schoepf UJ, et al. Comparison of dual-energy computed tomography of the heart with single photon emission computed tomography for assessment of coronary artery stenosis and of the myocardial blood supply. *Am J Cardiol*. 2009;104:318–326.

124. Wang R, Yu W, Wang Y, et al. Incremental value of dual-energy CT to coronary CT angiography for the detection of significant coronary stenosis: comparison with quantitative coronary angiography and single photon emission computed tomography. *Int J Cardiovasc Imaging*. 2011;27:647–656.

125. Ko SM, Choi JW, Hwang HK, Song MG, Shin JK, Chee HK. Diagnostic performance of combined noninvasive anatomic and functional assessment with dual-source CT and adenosine-induced stress dual-energy CT for detection of significant coronary stenosis. *AJR Am J Roentgenol*. 2012;198:512–520.

126. Jin KN, De Cecco CN, Caruso D, et al. Myocardial perfusion imaging with dual energy CT. *Eur J Radiol*. 2016;85:1914–1921.

127. So A, Hsieh J, Narayanan S, et al. Dual-energy CT and its potential use for quantitative myocardial CT perfusion. *J Cardiovasc Comput Tomogr*. 2012;6:308–317.

128. Bar E, Lalonde A, Royle G, Lu HM, Bouchard H. The potential of dual-energy CT to reduce proton beam range uncertainties. *Med Phys*. 2017;44:2332–2344.

129. Yang M, Virshup G, Clayton J, Zhu XR, Mohan R, Dong L. Theoretical variance analysis of single- and dual-energy computed tomography methods for calculating proton stopping power ratios of biological tissues. *Phys Med Biol*. 2010;55:1343–1362.

130. Yang M, Zhu XR, Park PC, et al. Comprehensive analysis of proton range uncertainties related to patient stopping-power-ratio estimation using the stoichiometric calibration. *Phys Med Biol*. 2012;57:4095–4115.

131. Saito M, Sagara S. Simplified derivation of stopping power ratio in the human body from dual-energy CT data. *Med Phys*. 2017;44:4179–4187.

132. Michalak G, Taasti V, Krauss B, Deisher A, Halaweish A, McCollough C. A comparison of relative proton stopping power measurements across patient size using dual- and single-energy CT. *Acta Oncol*. 2017;56:1465–1471.

133. Taasti VT, Michalak GJ, Hansen DC, et al. Validation of proton stopping power ratio estimation based on dual energy CT using fresh tissue samples. *Phys Med Biol*. 2017;63:015012.

134. Zhu J, Penfold SN. Dosimetric comparison of stopping power calibration with dual-energy CT and single-energy CT in proton therapy treatment planning. *Med Phys*. 2016;43:2845–2854.

135. Li B, Lee HC, Duan X, et al. Comprehensive analysis of proton range uncertainties related to stopping-power-ratio estimation using dual-energy CT imaging. *Phys Med Biol*. 2017;62:7056–7074.

136. Vilches-Freixas G, Taasti VT, Muren LP, et al. Comparison of projection- and image-based methods for proton stopping power estimation using dual energy CT. *Phys Imaging Radiat Oncol*. 2017;3:28–36.

137. Zhang S, Han D, Politte D, et al. TU-FG-BRB- 03: basis vector model based method for proton stopping power estimation from experimental dual energy CT data. *Med Phys*. 2016;43:3756–3756.

138. Zhang S, Han D, Politte DG, Williamson JF, O'Sullivan JA. Impact of joint statistical dual-energy CT reconstruction of proton stopping power images: comparison to image- and sinogram-domain material decomposition approaches. *Med Phys*. 2018;45:2129–2142.

139. Je E, Lee HH, Duan X, Li B, Jia X, Yang M. Optimal energy selection for proton stopping-power-ratio estimation using dual-energy CT-based monoenergetic imaging. *Phys Med Biol*. 2019;64:195015.

140. Wohlfahrt P, Mohler C, Hietschold V, et al. Clinical implementation of dual-energy CT for proton treatment planning on pseudo-monoenergetic CT scans. *Int J Radiat Oncol Biol Phys*. 2017;97:427–434.

141. Wohlfahrt P, Troost EGC, Hofmann C, Richter C, Jakobi A. Clinical feasibility of single-source dual-spiral 4D dual-energy ct for proton treatment planning within the thoracic region. *Int J Radiat Oncol Biol Phys*. 2018;102:830–840.

142. Michalak G, Grimes J, Fletcher J, et al. Technical Note: Improved CT number stability across patient size using dual-energy CT virtual monoenergetic imaging. *Med Phys*. 2016;43:513.

143. Jacobsen MC, Schellingerhout D, Wood CA, et al. Intermanufacturer comparison of dual-energy CT iodine quantification and monochromatic attenuation: a phantom study. *Radiology*. 2018;287:224–234.

144. Rodriguez-Granillo GA, Carrascosa P, Cipriano S, et al. Beam hardening artifact reduction using dual energy computed tomography: implications for myocardial perfusion studies. *Cardiovasc Diagn Ther*. 2015;5:79–85.

145. Scheske JA, O'Brien JM, Earls JP, et al. Coronary artery imaging with single-source rapid kilovolt peak-switching dual-energy CT. *Radiology*. 2013;268:702–709.

146. Stolzmann P, Winklhofer S, Schwendener N, Alkadhi H, Thali MJ, Ruder TD. Monoenergetic computed tomography reconstructions reduce beam hardening artifacts from dental restorations. *Forensic Sci Med Pathol*. 2013;9:327–332.

147. Bamberg F, Dierks A, Nikolaou K, Reiser MF, Becker CR, Johnson TR. Metal artifact reduction by dual energy computed tomography using monoenergetic extrapolation. *Eur Radiol*. 2011;21:1424–1429.

148. Cha J, Kim HJ, Kim ST, Kim YK, Kim HY, Park GM. Dual-energy CT with virtual monochromatic images and metal artifact reduction software for reducing metallic dental artifacts. *Acta Radiol*. 2017;58:1312–1319.

149. Dunet V, Bernasconi M, Hajdu SD, Meuli RA, Daniel RT, Zerlauth JB. Impact of metal artifact reduction software on image quality of gemstone spectral imaging dual-energy cerebral CT angiography after intracranial aneurysm clipping. *Neuroradiology*. 2017;59:845–852.

150. Filograna L, Magarelli N, Leone A, et al. Value of monoenergetic dual-energy CT (DECT) for artefact reduction from metallic orthopedic implants in post-mortem studies. *Skeletal Radiol*. 2015;44:1287–1294.

151. Guggenberger R, Winklhofer S, Osterhoff G, et al. Metallic artefact reduction with monoenergetic dual-energy CT: systematic ex vivo evaluation of posterior spinal fusion implants from various vendors and different spine levels. *Eur Radiol*. 2012;22:2357–2364.

152. Yue D, Fan Rong C, Ning C, et al. Reduction of metal artifacts from unilateral hip arthroplasty on dual-energy CT with metal artifact reduction software. *Acta Radiol*. 2017;59:853–860.

153. Zhou C, Zhao YE, Luo S, et al. Monoenergetic imaging of dual-energy CT reduces artifacts from implanted metal orthopedic devices in patients with factures. *Acad Radiol*. 2011;18:1252–1257.

154. Grajo JR, Sahani DV. Dual-energy CT of the abdomen and pelvis: radiation dose considerations. *J Am Coll Radiol*. 2018;15:1128–1132.

155. Renapurkar RD, Primak A, Azok J, et al. Attenuation-based kV pair selection in dual source dual energy computed tomography angiography of the chest: impact on radiation dose and image quality. *Eur Radiol*. 2017;27:3283–3289.

156. Uhrig M, Simons D, Kachelriess M, Pisana F, Kuchenbecker S, Schlemmer HP. Advanced abdominal imaging with dual energy CT is feasible without increasing radiation dose. *Cancer Imaging*. 2016; 16:15.

157. Zhu X, McCullough WP, Mecca P, Servaes S, Darge K. Dual-energy compared to single-energy CT in pediatric imaging: a phantom study for DECT clinical guidance. *Pediatr Radiol*. 2016;46:1671–1679.

158. Matsubara K, Takata T, Kobayashi M, Kobayashi S, Koshida K, Gabata T. Tube current modulation between single- and dual-energy CT with a second-generation dual-source scanner: radiation dose and image quality. *AJR Am J Roentgenol*. 2016;207:354–361.

159. Michalak G, Grimes J, Fletcher JG, et al. Selection of optimal tube potential settings for dual-energy CT virtual mono-energetic imaging of iodine in the abdomen. *Abdom Radiol*. 2017;42:2289–2296.

160. Boone JM. Dose spread functions in computed tomography: a Monte Carlo study. *Med Phys*. 2009;36:4547–4554.

161. Dixon RL, Munley MT, Bayram E. An improved analytical model for CT dose simulation with a new look at the theory of CT dose. *Med Phys*. 2005;32:3712–3728.

162. International Electrotechnical Commission. Medical electrical equipment - Part 2-44: Particular requirements for the basic safety and essential performance of x-ray equipment for computed tomography (IEC 60601-2-44; Edition 3.2). Geneva, Switzerland; 2016.

163. International Commission on Radiological Protection. *Recommendations of the International Commission on Radiological Protection (ICRP #26)*. Oxford: The International Commission on Radiological Protection; 1977. ICRP Publication 26.

164. International Commission on Radiological Protection. 1990 Recommendations of the International Commission on Radiological Protection (ICRP Publication 60); 1991. 60.

165. Jones DG, Shrimpton PC. *Survey of CT Practice in the UK. Part 3: Normalised Organ Doses Calculated using Monte Carlo Techniques*. Oxon: National Radiological Protection Board; 1991.

166. Zankl M, Panzer W, Drexler G. The calculation of dose from external photon exposures using reference human phantoms and Monte Carlo methods. Part VI: Organ doses from computed tomographic examinations. Neuherberg, Germany: GSF - Forschungszentrum fur Umwelt und Gesundheit, Institut fur Strahlenschutz; 1991. GSF-Bericht 30/91.

167. Bongartz G, Golding SJ, Jurik AG, et al. European guidelines for multislice computed tomography. European Commission (Contract Number FIGM-CT2000-20078-CT-TIP); 2004. http://www.drs.dk/guidelines/ct/quality/index.htm

168. European Commission. European guidelines on quality criteria for computed tomography (EUR 16262 EN). Available at: http://www.drs.dk/guidelines/ct/quality/mainindex.htm. Luxembourg: European Commission & The Office For Official Publications of the European Communities;2000. EUR 16262 EN.

169. Jessen KA, Shrimpton PC, Geleijns J, Panzer W, Tosi G. Dosimetry for optimisation of patient protection in computed tomography. *Appl Radiat Isot*. 1999;50:165–172.

170. Shrimpton PC. Reference doses for computed tomography. *Radiol Protect Bull*. 1997;193:16–19.

171. Shrimpton PC, Hillier MC, Lewis MA, Dunn M. Doses from computed tomography (CT) examinations in the UK: 2003 review. National Radiological Protection Board; 2005. http://www.biophysicssite.com/Documents/NRPB_W67/NRPB_W67.pdf

172. Christner JA, Kofler JM, McCollough CH. Estimating effective dose for CT using dose-length product compared with using organ doses: consequences of adopting International Commission on Radiological Protection publication 103 or dual-energy scanning. *AJR Am J Roentgenol*. 2010;194:881–889.

173. Mattison BJ, Nguyen GB, Januzis N, Lowry C, Yoshizumi TT. A novel approach for effective dose measurements in dual-energy CT. *Radiat Prot Dosimetry*. 2016;172:416–421.

174. Paul J, Banckwitz R, Krauss B, Vogl TJ, Maentele W, Bauer RW. Estimation and comparison of effective dose (E) in standard chest CT by organ dose measurements and dose-length-product methods and assessment of the influence of CT tube potential (energy dependency) on effective dose in a dual-source CT. *Eur J Radiol*. 2012;81:e507–e512.

175. Schenzle JC, Sommer WH, Neumaier K, et al. Dual energy CT of the chest: how about the dose? *Invest Radiol*. 2010;45:347–353.

176. McCollough CH, Yu L, Kofler JM, et al. Degradation of CT low-contrast spatial resolution due to the use of iterative reconstruction and reduced dose levels. *Radiology*. 2015;276:499–506.

177. Yu L, Vrieze TJ, Leng S, Fletcher JG, McCollough CH. Technical Note: Measuring contrast- and noise-dependent spatial resolution of an iterative reconstruction method in CT using ensemble averaging. *Med Phys*. 2015;42:2261–2267.

178. Leng S, Yu L, Wang J, Fletcher JG, Mistretta CA, McCollough CH. Noise reduction in spectral CT: reducing dose and breaking the trade-off between image noise and energy bin selection. *Med Phys*. 2011;38:4946–4957.

179. Bruder H, Raupach R, Sunnegardh J, et al. Novel iterative reconstruction method with optimal dose usage for partially redundant CT-acquisition. *Phys Med Biol*. 2015;60:8567–8582.

180. Bellini D, Gupta S, Ramirez-Giraldo JC, et al. Use of a noise optimized monoenergetic algorithm for patient-size independent selection of an optimal energy level during dual-energy CT of the pancreas. *J Comput Assist Tomogr*. 2017;41:39–47.

181. Petrongolo M, Zhu L. Noise suppression for dual-energy CT through entropy minimization. *IEEE Trans Med Imaging*. 2015;34:2286–2297.

182. Nute JL, Jacobsen MC, Stefan W, Wei W, Cody DD. Development of a dual-energy computed tomography quality control program: characterization of scanner response and definition of relevant parameters for a fast-kVp switching dual-energy computed tomography system. *Med Phys*. 2018;45:1444–1458.

183. Foley WD, Shuman WP, Siegel MJ, et al. White paper of the society of computed body tomography and magnetic resonance on dual-energy CT, part 2: radiation dose and iodine sensitivity. *J Comput Assist Tomogr*. 2016;40:846–850.

184. Delesalle MA, Pontana F, Duhamel A, et al. Spectral optimization of chest CT angiography with reduced iodine load: experience in 80 patients evaluated with dual-source, dual-energy CT. *Radiology*. 2013;267:256–266.

185. Dong J, Wang X, Jiang X, et al. Low-contrast agent dose dual-energy CT monochromatic imaging in pulmonary angiography versus routine CT. *J Comput Assist Tomogr*. 2013;37:618–625.

186. Yuan R, Shuman WP, Earls JP, et al. Reduced iodine load at CT pulmonary angiography with dual-energy monochromatic imaging: comparison with standard CT pulmonary angiography–a prospective randomized trial. *Radiology*. 2012;262:290–297.

187. Pansini M, Morsbach F, Schubert T, et al. Feasibility of dose optimization in a second-generation dual-source CT scanner for a manufacturer-recommended urolithiasis protocol for imaging renal stones. *AJR Am J Roentgenol*. 2016;206:348–354.

188. Qu M, Yu L, Cardona DG, et al. Radiation dose reduction in dual-energy ct: does it affect the accuracy of urinary stone characterization? *AJR Am J Roentgenol*. 2015;205:W172–W176.

189. Johnson TR. Dual-energy CT: general principles. *AJR Am J Roentgenol*. 2012;199:S3–S8.

190. Lehmann LA, Alvarez RE, Macovski A, et al. Generalized image combinations in dual Kvp digital radiography. *Med Phys*. 1981;8:659–667.

APPENDIX

AAPM:	American Association of Physicists in Medicine
AEC:	Automatic exposure control
ALARA:	As Low As Reasonably Achievable
Atomic number (Z):	The number of protons in the nucleus
Basis materials:	At a given energy, materials have unique photoelectric and Compton effects. Such materials, known as basis materials, must have sufficiently different attenuation characteristics to be used for material decomposition
Beam filtration CT:	Low- and high-energy are obtained from a single, polychromatic x-ray source with a split pre-filter in the longitudinal direction
Beam hardening:	A consequence of a polychromatic x-ray source where low energy photons are preferentially attenuated in a medium compared to high energy photons
CNR:	Contrast to noise ratio
Coherent scatter:	Incident photon interacts with an atom resulting in an excited atom that immediately emits a photon of the same energy but in a different direction. Also known as Rayleigh scatter
Compton scatter:	Incident photon interacts with a valence electron of an atom, which is ejected from the atom. The scattered photon is emitted with a reduction in energy and in a different direction
CT number:	The quantitative value used to represent the gray scale values in a CT image. Defined as: $$\mathrm{CT\,Number} = 1000\,\frac{\mu(x,y,z) - \mu_W}{\mu_W},$$ where $\mu(x,y,z)$ is the average linear attenuation coefficient in a voxel and μ_W is the linear attenuation coefficient for water at a specified energy.
CTDI:	Computed Tomography Dose Index
CTR:	CT number ratio
DECT:	Dual-energy computed tomography
DLP:	Dose-length product
Dual-layer detector:	A detector that uses two layers of energy-integrating scintillators to measure the low- and high-energy data
Dual-source CT:	A CT system with two x-ray tube and detector pairs off-set from each other at about 90°. Each x-ray tube can be operated at different tube potential settings and additional pre-filtration can be added for one of the tubes to improve spectral energy separation
Effective atomic number (Z_{eff}):	A description of the average atomic number for a heterogenous material
Effective dose:	A radiation protection metric that conveys the radiation detriment from a partial body irradiation in terms of a whole body irradiation with equivalent detriment. This population metric is neither age nor gender specific and cannot be used to estimate the risk to a specific patient. It is typically used to compare the relative risk between various radiological studies
HU:	Hounsfield Unit. The unit associated with CT number
ICRP:	International Commission on Radiological Protection
ICRU:	International Commission on Radiation Units & Measurements
Image-space material decomposition:	Material decomposition process is performed using only reconstructed image data

Linear attenuation coefficient (μ):	The fraction of photons removed from a monoenergetic beam per unit thickness of material, represented in cm^{-1} $\mu = \dfrac{n}{N\Delta x}$, where n is the number of photons removed from the beam, N is the number of incident photons and x is the thickness of the material.
Linear attenuation ratio (LAR):	Ratio of the linear attenuation coefficients from two energy levels that may be used to calculate the effective atomic number from a calibration plot
Mass attenuation coefficient (μ/ρ):	The linear attenuation coefficient normalized to the density of a given material, represented in units of cm^2/g
Material decomposition:	Process to represent a material of interest as a mixture or linear combination of known material attenuation functions or basis materials
Material-specific images:	CT images generated from material decomposition that represent the distribution of a material of interest.
MECT:	Multienergy computed tomography
MOSFET:	Metal-oxide-semiconductor field-effect transistor
Multi-material decomposition:	Material decomposition using more than 3 basis materials
NIST:	National Institute of Standards and Technology
OSL:	Optically stimulated luminescence
Photoelectric effect:	Incident photon is completely absorbed by an atom and an electron (photoelectron) is ejected
Photon counting detector CT:	A CT system that utilizes semi-conductor detectors to directly convert x-rays into short voltage pulses whose heights are approximately proportional to the x-ray energies. The pulses are individually counted when they exceed a given threshold
Projection-space material decomposition:	Material decomposition process is performed prior to image reconstruction using projection data; this requires knowledge of the input x-ray spectra, beam shaping filter (e.g., bowtie filter) and spectral response of the x-ray detector(s)
Single energy CT:	Conventional CT using a single energy spectrum for data acquisition
Sinogram:	The CT projection data at different angles transformed into a 2-D representation
Three-material decomposition:	Material decomposition using three basis materials
TLD:	Thermoluminescent dosimeter
Total mass attenuation coefficient:	Summation of the mass attenuation coefficients (μ/ρ) of x-ray interactions with matter $\left(\dfrac{\mu}{\rho}\right)_{Total} = \left(\dfrac{\mu}{\rho}\right)_{Photoelectric} + \left(\dfrac{\mu}{\rho}\right)_{Compton} + \left(\dfrac{\mu}{\rho}\right)_{Coherent}$
Tube potential switching (fast kV switching):	Low- and high-energy data are collected by rapidly switching the tube potential between low and high settings
Virtual monoenergetic images (VMI):	Synthetic images created from material decomposition data (mass density and effective atomic number) and monoenergetic attenuation coefficient information to mimic the appearance of images generated with a monoenergetic x-ray source.
Virtual non-calcium (VNCa) images:	Material selective images with the calcium equivalent signal removed
Virtual non-contrast (VNC) images:	Material selective images with the iodine equivalent signal removed. Soft-tissue, fat and iodine are the basis materials.